




A comprehensive study on the influence of the scan pattern in two porosity levels and surface roughness on the fatigue behavior of laser powder bed fusion manufactured specimens made of steel H13

J. Zhang^{1,2,*} , J. Schumacher¹, and B. Clausen^{1,2}

¹IWT - Leibniz-Institut für Werkstofforientierte Technologien, Badgasteiner Str. 3, 28359 Bremen, Germany

²Faculty of Production Engineering, University of Bremen, Badgasteiner Str. 1, 28359 Bremen, Germany

Received: 14 April 2023

Accepted: 25 April 2023

Published online:

19 June 2023

© The Author(s) 2023

ABSTRACT

As a developing and immature technique, additive manufacturing (AM) shows some limitations: depending on material and process parameters so far, it usually results in parts with residual porosity, high residual stresses and a surface with a certain level of roughness. Due to its weaknesses and high production costs, AM is more preferably used when the fabricated parts have a high geometry complexity, the material used is very expensive, or the parts can offer additional performance. In order to allocate AM further in industry, a better understanding of the not well-investigated fatigue behavior is necessary. This work focuses on the influences of some general process parameters including laser power, scan speed, scan pattern and postmachining on the resulting fatigue properties of H13 tool steel specimens generated through powder bed fusion (PBF) technique. Results reveal that scan patterns influence fatigue properties by affecting the largest porous defect size and microstructure thus matrix strength. The degree of porosity or roughness resulting from the energy input and postmachining has a significant inferior impact on the fatigue strength. Neither porosity nor tensile properties show a single direct mathematic correlation with the fatigue properties.

Handling Editor: Sophie Primig.

Address correspondence to E-mail: zhang@iwt-bremen.de; clausen@iwt-bremen.de

Introduction

As a developing production technique, creating an object in a layerwise manner, *additive manufacturing (AM)* can be classified into seven categories according to different working mechanisms [1]. Among them four categories, i.e., *Binder Jetting (BJ)*, *Sheet Lamination (SL)*, *Direct Energy Deposition (DED)* and *Powder Bed Fusion (PBF)* are commonly used for the production of metallic materials, while *DED* and *PBF* are the two processes most frequently applied for metal products. Compared to *DED* with its focus and convenience on maintenance, *PBF* is more preferably employed for series production of material parts [2]. Based on the energy source used, *PBF* is further categorized into *electron beam powder bed fusion (PBF-EB/M)* and *laser powder bed fusion (PFB-LB/M)*. For some metal productions which require preheating of the platform to reduce temperature gradient, *PBF-EB/M* usually generates higher preheating temperatures over than 800 °C [3, 4], while *PFB-LB/M* has a wider preheating temperature range from no preheating up to 1000 °C. As a result, *PFB-LB/M* reveals more advantages over other *AM* techniques to produce metallic parts.

AISI H13 (X40CrMoV5-1) is a medium carbon tool steel with carbon content ranging from 0.32% to 0.45%. As a high strength tool steel featured with superior thermal properties, it is commonly used in high working temperature environments such as die casting, forging, injection or extrusion. However, the rapid changes in manufacturing require more complicated and diversified geometries of tools. In contrast to conventional manufacturing which is at very high expense for complex geometries, *AM* or particularly *PFB-LB/M* is an optimal substitute for producing workpieces with highly increasing geometrical requirements.

The microstructure of H13 produced by *PFB-LB/M* is composed of dendrites/solidification cells [5] and interdendritic regions which are enriched with retained austenite and microsegregation of alloying elements like Cr, Mo and V [5, 6]. Depending on local temperature gradients within the melt pool due to the fast solidification from the *PFB-LB/M* process, three grain structures, i.e., fine/coarse, cellular and columnar grains, are observed in H13 [7]. Additionally clusters, defined as domains with all neighboring (sub-) grains of the same grain structure being characterized by similar growth direction and orientation

as well as the ratio of length to width, are identified [4]. Low-angle grain boundaries (LAGBs) arise between the sub-grains, while high-angle grain boundaries (HAGBs) turn up between these clusters [4]. Owing to the rapid solidification rate and local carbon enrichments, the resulting microstructure contains a high amount of retained austenite in a range from 10 to 15% [8–10]. Some researchers [11, 12] investigated the solidification process and proposed that the cellular grains contain α/α' -Fe with γ -Fe located at the boundaries. Wu and Deirmina et al. confirmed this by EBSD mapping [4, 5, 13]. The cellular structure is a consequence of the rapid solidification and microsegregation of alloying elements in the interdendritic regions. During the rapid cooling segregation of heavy elements at the cellular/dendrite sub-grains are promoted [8] and carbon diffusion is impeded [14–16]. The heavy elements forming carbides, aggregate at the border of C-rich regions in the cellular boundaries [14]. With carbon being a strong austenite stabilizer, the remaining still high carbon content facilitates the maintaining of austenite at the grain boundaries [4]. Concerning the crystallographic texture in *PFB-LB/M* generated H13 not much information is available in the literature, which suggests that the texture structure may be unapparent in *PFB-LB/M* process [5, 17].

The common defects arising from *PFB-LB/M* process contain a certain level of surface roughness, keyhole pores, cavities, lack of fusions and material property-dependent residual stresses. Besides the typical defects from the *PFB-LB/M* process, for carbon tool steels some other specific defects, mainly different types of cracks, turn up. The first two residual stress crack types, i.e., fatigue-like and bending-like residual stress cracks, are macroscopic cracks based on different residual stress evolutions with individual morphology [4]. The residual stresses consist of thermal and structural parts where the structural part originates from austenite martensite transformation in the carbon tool steel. The structural stresses are highly influenced by the local carbon content [18, 19]. During consecutive depositions of layers, repeated heating and cooling take place, which lead to cyclic residual stresses. For tool steels with a carbon content less than 0.5%, like H13, the limited evolution of cyclic residual stresses [20] results in cracks initiating mostly from the parts surface and progressing in a wave-like manner in small steps parallel to the horizontal direction, without macroscopic deformation.

The well-known macroscopic horizontal cracks from steep temperature gradients belong to this crack group and can be avoided by suitably increasing the preheating temperature, which is usually higher than 100 °C [4, 10, 21]. For high carbon tool steel with a carbon content higher than 1%, the high cyclic residual stresses [20] generate vertically propagating bending-like cracks, which finally cause severe macroscopic bending of the part. The third crack type is named as microscopic vertical welding-like centerline hot cracks [4], which are the same as the hot cracks from the welding process [22, 23] and are caused by the particularly high energy input and appear in the center of the melt pool. The last type is called microscopic vertically aligned solidification cracks [4], which are the result of a high degree of element segregation and thus arise at the cluster interfaces. It is a typical phenomenon arising from welding process, where at the terminal solidification stage due to constrained liquid feeding the semisolid films at dendritic grain boundaries fractures [24–26]. Xia and Kou et al. found out from welding experiments that tool steel has a cracking susceptibility with a minimum carbon content of 0.2 wt% and the susceptibility increases rapidly with increasing carbon content [27]. Owing to the high similarity between fusion welding and fusion additive manufacturing, solidification cracks are also reported in PBF-LB/M generated H13 [26, 28], as well as some various types of alloys processed by PBF-LB/M, like nickel-based superalloy [29], FeCrAl alloy [30], aluminum alloys [31], aluminum alloys nickel base alloy [32], magnesium alloys [33], high-entropy alloys [34]. Solidification cracks and welding-like centerline hot cracks look similar, but differ in the formation mechanisms and positions [4]. The welding-like centerline hot cracks are independent of the chemical compositions, while solidification cracks are independent on the laser parameter settings. In short, defects referred to appear under optimized process parameters in H13 are keyhole pores, irregular cavities at melt pool level, vertically distributed hot and solidification cracks, and horizontally located lack of fusions.

Due to the use of AISI H13 as structural components, the mechanical properties are of outstanding importance. Because of the different microstructure morphologies of PFB-LB/M generated H13 compared to its conventional counterparts, the mechanical performance is assumed to be different. Also, the likely occurring diversified groups of defects in PFB-

LB/M processed H13 lead to a severe restriction and deterioration to the mechanical properties. Yan and Mazur et al. reported very high compressive residual stresses in PFB-LB/M produced H13 from 900 to 1500 MPa in the range of yield strength [35, 36]. Some studies reported an enhanced hardness in a range from 561 HV [17] to 894 HV [10] due to a finer martensitic microstructure. Hardness values in between like 748 ± 28 HV [37] were also obtained by many researchers. Both refined microstructure and enhanced hardness are considered to be beneficial factors for the mechanical strengths. Other research works about the static properties of PFB-LB/M manufactured H13 observed differences in tensile behaviors compared with the conventional counterparts. Holzweissig et al. [21] noticed work hardening behavior occurring at lower stresses in PFB-LB/M H13 due to the beginning transformation of retained austenite into martensite. All PFB-LB/M specimens broke in a brittle manner without necking [7, 10, 17], whereas the conventional steel H13 (abbreviation CS H13) deforms at higher yield strengths and fractures after necking. The porous defects and the interfaces between different phases or microstructural structures were considered to be crack origins for the tensile fracture. Current researches referenced tensile strengths mostly from 835 [10] to 1700 MPa [15] and noticeably lower elongations from 1.6 [15] to 4.1% [10]. Moderate strength 1550–1650 MPa [21] and ductility 2–2.25% [21] were reported by many researchers. The maximum value of 1700 MPa reported for the tensile strength is comparable to conventional values. However, increasing tensile strengths generally occur at the expense of reduced ductility. Concerning the elongation range two outliers reported remarkably higher elongations of 12.4% [17] and 12.9% [14]. 12.9% is prominently higher than the conventional ductility of H13.

When comparing the H13 samples manufactured by DED and LPB-EB/M, both methods present a lath-shaped martensite microstructure with some amount of retained austenite. DED leads to larger solidification cells with sizes ranging from 2 to 30 μm ([38–42] as quoted in [5]) and more remarkable secondary dendritic arms [42], compared to 0.5 to 2 μm cell sizes in LPB-LB/M ([11, 17, 21, 36] as quoted by [5]). A pronounced in situ tempering effect is observed in DED induced by the intrinsic heat treatment (IHT) from the subsequent layer processes. The top layer has little IHT influence, displaying higher hardness

([42–45] as quoted by [5]), while the lower layers experience significant IHT effect, showing lower hardness with tempered martensite and V, Cr-rich carbides. Due to decreased cooling rate and heat conduction during the build, the cells are larger at the top than the ones at the bottom in *DED* [46]. The IHT is also reported for *PBF-LB/M* [10, 13], which is however not as conclusive as in *DED*. Deirmina et al. proposed a low-temperature transformation during the *PBF-LB/M* upon findings in his work [13]. Higher hardness in the top layer is also observed for *PBF-LB/M* without or with preheating up to 200 °C [10]. Compared to the generally similar or higher hardness, however, significantly lower yield and tensile strength and elongation at fracture of H13 produced by *PBF-LB/M* than the CS H13, *DED* generated H13 shows similar hardness (550 to 660 HV) [42, 45, 47], tensile strength (~ 2000 MPa) and fracture elongation (5–6%) compared to the CS H13, which is attributed to the strong in situ tempering effect [40]. Compared to the *PBF-LB/M* with a rapid cooling rate (up to 10^6 K/s [48]), *PBF-EB/M* has a relatively slow cooling speed due to the high pre-heating temperature. The resulting fine needle-like microstructure consists of martensite and a high fraction of bainite, as is more similar to the CS H13. Vanadium enriched precipitates are present in the microstructure, and the amount of retained austenite is below 5% [49]. The IHT in *PBF-EB/M* leads to a few solid to solid phase transformations and an effect of grain refinement before the bainite/martensite transformation. The IHT brings in annealing and therefore changes like austenite coarsening in the lower layers. The corresponding hardness increases with increasing height (500 to 580 HV), with the top layer being characterized with the highest hardness. *PBF-EB/M* generated H13 demonstrates much lower yield strength (~ 1100 MPa) with noticeable hardening after initial yielding and around 150 MPa lower tensile strength, however, a remarkably higher elongation at fracture (13%), compared to 1650 MPa yield strength, 1990 MPa tensile strength and 9% fracture elongation in the CS H13 [10].

So far works were mainly focused on static properties and there are less publications on the dynamic properties; however, most structural components mainly experience cyclic loadings in reality. Comprehensive investigations of the mechanical properties, especially on the fatigue properties of *PBF-LB/M* generated H13, are still ongoing, and the conclusive

summaries have not been made. Previous work of Mazur et al. [35] reported significant lower fatigue strength of perpendicularly *PBF-LB/M* generated dense H13 samples (99.88%) with as-built surface finish than the CS H13 (around 100 MPa compared to 760 MPa), which is attributed to the rough surface and high compressive residual stresses with an average value of 1150 MPa. The fatigue strength increases substantially after stress relief treatment. Recent work by Garcias et al. [50] revealed also a tremendously deduction of 80% lower fatigue strength in vertically *PBF-LB/M* produced H13 with polished surface finish (fatigue limit of 38 MPa at 2×10^6 cycles compared to 205 MPa), which were designed to have maximum stresses displayed at reduced section with minimum weight and amount of powder consumed, as compared to its conventional counterparts. The *PBF-LB/M* fatigue samples showed a general defect dimension from 50 to 500 μm , while the fracture surfaces of conventional H13 displayed critical defects sizes between 50 and 80 μm or some even smaller than 50 μm . The corresponding 8% porosity acted as the primary defects and as well the origins for fatigue fracture, with the presence of lack of fusion at the same time. In another work by Pellizzari et al. [51] similar conclusion that inferior fatigue properties of *PBF-LB/M* produced H13 than the CS H13 (two times lower) were observed due to the presence of lack of fusion as the dominant crack initiation sites. Post-treatment like tempering and turning can balance the properties between tensile strength and toughness. The fatigue strength was accordingly affected by the defect size, shape, and location, which were influenced by the building direction, and therefore resulted in a high scatter and anisotropy of the properties. Horizontally built samples display better fatigue properties than samples built under 45° and 90°, owing to its smaller defect sizes in the area perpendicular to the main stress axis. A further investigation specifically on the fatigue fracture morphology of vertically *PBF-LB/M* generated H13 samples by Macek et al. [52] illustrated a predominant transgranular fracture mechanism for high cycle fatigue loaded samples, where pores and unmelted particles promote the fracture process. Scanning Electron Microscopy (SEM) fractography investigations of the fracture surfaces exhibited a pore size ranging from 0.08 to 0.15 mm. The fracture tomography and porosity along the sample axis were influenced by the different loading

stress levels, i.e., the higher the loading stress, the coarser and more uniform porosity appeared on the fracture surface, which was due to the domination of ductile fracture type.

In this study, an overall investigation on the influences of porosity, surface roughness and scan pattern, on the fatigue properties of H13 specimens was conducted. This investigation was carried out via metallographic investigations and mechanical testing of various *PBF-LB/M* process routes of H13. Simultaneously, conventionally processed H13 was examined as a reference state.

Materials and methods

PBF-LB/M manufacturing

The *PBF-LB/M* manufacturing of H13 tool steel was conducted on a ReaLizer SLM 250 machine (ReaLizer, Borchten, Germany) in a building space with a size of 250 mm × 250 mm × 250 mm. A single continuous mode IPG YLR-200 SM-CW fiber laser beam with standard diameter of 50 μm and maximum 200 W power and 1073 μm wave length is implemented in the machine. Argon was applied as protect gas for the manufacturing. To reduce the process generated residual stresses, a preheating of 240 °C was conducted via a thermocouple within the build platform. The H13 tool steel powder with a spherical form was provided by new materials development GmbH. The size distribution data are $D_{10} = 10.21 \mu\text{m}$, $D_{50} = 29.35 \mu\text{m}$, $D_{90} = 48.05 \mu\text{m}$. Table 1 shows the chemical composition of the CS H13 and the powder used in this study. A previous measurement by inert gas fusion in this research work [53] shows the respective oxygen content in the CS H13 and the H13 powder is 0.0013% and 0.0541%. Tensile and fatigue specimens were generated with varying process parameters and scan strategies as follows:

Two different sets of process parameters (laser power, scan speed, etc.) of stripe scan pattern with a 10 mm length of scan vector (S10) were explored. The two parameter sets generate samples with a high and lowest known porosity states. Three variants of tensile and fatigue specimens were produced horizontally, under a polar angle of 0°. The first with the high porosity level and turned surface (S10, 0°, high porosity, turned). The second variant with lowest possible porosities and as-built surface (S10, 0°, low

porosity, as-built). The third like the second but with turned surface (S10, 0°, low porosity, turned), to study the influences of porosity and surface roughness. For variants with turned surface, a stock allowance of 0.2 mm was prepared for the surface removal. Seven tensile samples for the two variants with lowest possible porosities and six fatigue specimens for all three variants were fabricated (Table 2). It needs to be noticed that for the variant with high porosity no tensile specimens were produced. The specimens were built up horizontally with 0° polar angle. The powder layer thickness for all and further variants was fixed to 50 μm. The complete pattern of each layer was rotated with 79° for every subsequent layer for all and further variants to minimize possible texture microstructure and for less anisotropic behavior. The support structure of all three variants was manually removed. Afterward, the two variants with turned surface were further machined to obtain a smooth surface.

The previous explored process parameters with the lowest porosity were further applied to generate two further variants with different scan patterns. One variant with stripe pattern with 3 mm scan vector lengths (S3, 0°, low porosity, turned). Another variant with chessboard pattern with alternating tiles of a 3 mm track length (C3, 0°, low porosity, turned). All samples were built up horizontally with a polar angle of 0°. Each variant contained in total six tensile and 20 fatigue specimens. Due to the limitation of manufacturing space, variants S10, S3 and C3 of low porosity consist of two or three batches, which were generated separately. Three cubes with a side length of 10 mm were produced for each variant for the metallographic investigations including microstructure, hardness, porosity and phase distribution. The geometries of the tensile, fatigue and cube specimens are given in Fig. 1. The manufacturing parameters and the number of usable samples for each variant are shown in Table 2.

Characterization and testing methods

To characterize the microstructural features, two cubes were employed for a preliminary metallographic examination on the influence of scan parameters on concerning the microstructure, hardness and porosity. For the metallographic investigations, the cross sections were obtained through cutting the uprightly established cubes with

orientation perpendicular to x abscissa, as illustrated in Fig. 1c. The microstructure and porosity were determined through a Axioplan II optical microscope (Zeiss, Oberkochen, Germany) and an image analysis optical microscope DMX (Leica, Wetzlar, Germany). The Vickers hardness (HV1) was measured with a 10×10 data point matrix via a LV-700 AT testing device (LECO, Mönchengladbach, Germany). Additionally, an X-ray diffraction analysis (XRD) was performed on one C3 cube section with an X-ray diffractometer composed of an “analytical X-ray MZ VI E” goniometer (GE Inspection Technologies, Ahrensburg, Germany), an ID 3003 generator (GE, Ahrensburg, Germany) and a position-sensitive detector (PSD) “Miostar II” detector (Photron-X, Ottobrunn, Germany) to get to know the phases being generated after *PBF-LB/M*. Also, a wavelength-dispersive X-ray spectroscopy (WDXS) measurement was taken on one later fatigue tested specimen from S10 (batch 1) with a device JXA-8200 (JEOL, Freising, Germany). It was used to analyze the distributions and segregations of elements V, Cr and Mo. Additionally, a transverse section of this later fatigue investigated specimen from S10 (batch 1) and several longitudinal cross sections of each variant were investigated with optical microscope to understand the different fatigue failures.

The third cube was used for density determination by Archimedes method with a density determination kit YDK01 (Sartorius, Göttingen, Germany). The roughness, conveyed in form of the maximal height S_{zz} , of as-built *PBF-LB/M* and turned surfaces for fatigue specimens was measured by a VK-9700 3D laser scan color microscope (Keyence, Neu-Isenburg, Germany). For the as-built *PBF-LB/M* surface, four roughness values for upper, lateral and underside faces were taken. The value for the bottom side, where the support structure was removed, is marked as roughness of underside. The values for the top and side faces were averaged and noted as roughness for the remaining sides. For the turned surface two values were taken for the top and bottom sides each and the average value was rated as roughness for the turned surface.

The mechanical characterizations were conducted through an electron mechanical tensile testing device RM250 (Schenck, Darmstadt, Germany) and via an electro-magnetic resonance fatigue testing machine type 2HFP (Amsler, Schaffhausen, Switzerland). The fatigue experiments were achieved through a

tension–compression load-controlled dynamic test under a stress ratio $R = -1$ and a material stiffness-controlled resonant frequency of 125 ± 13 Hz. A boundary limit of cycle numbers was set as 10 million. If after 10 million cycles the specimen still not failed, it was assessed as run out. These samples were subjected to higher fatigue loading until fracture, to be able to determine their weak points as well. Stair case method was applied to quickly approach the rough range of fatigue limit. Thereafter the fatigue tests were further conducted at several stress levels within the fatigue limit range with one to four sample each to gain the corresponding fracture possibility. The fracture probability $P_F(\sigma_a)$ at stress level σ_a is defined as the number of the specimens failed $n_F(\sigma_a)$ divided by the total number of the samples $n_T(\sigma_a)$, as given in Eq. (1).

$$P_F(\sigma_a) = \frac{n_F(\sigma_a)}{n_T(\sigma_a)} \quad (1)$$

A two-parametric Weibull distribution function, as revealed in Eq. (2), was employed to statistically describe the fracture probability $P_F(\sigma_a)$ by calibrating the parameters.

$$P_F(\sigma_a) = 1 - 2^{-\left(\frac{\sigma_a}{\sigma_w}\right)^m} \quad (2)$$

The scale parameter σ_w and shape parameter m represent a medium fatigue limit value with a 50% fracture possibility and the slope of the distribution curve, respectively.

For the purpose of assessing the diverse fatigue failures, all fatigued samples of *PBF-LB/M* produced H13 and only the fractured conventional H13 specimens were subjected to examine the fracture surfaces under a Vega II XLH scanning electron microscope (Tescan, Dortmund, Germany, abbreviation SEM) to obtain the weak point of each specimen. The weak point where crack originated was further evaluated by a software ImageJ to acquire its size and position information. A Fréchet distribution function, as shown in Eq. (3),

$$F_{\text{defect size}}(d) = P(\text{defect size} \leq d) = 2^{-\left(\frac{d}{d_m}\right)^c} \quad (3)$$

with the scale and shape parameters d_m and c is adopted to fit the statistical data of the size distribution of all the weak points.

Furthermore, according to Murakami [54] the fatigue limit σ_w , as a function of the largest defect size $\sqrt{\text{area}}$ as displayed in Eq. (4), is applied to a

Table 1 Chemical composition of conventional H13 steel and AISI H13 powder for *PBF-LB/M* manufacturing in mass fraction %

Variant	C	Cr	Mo	V	Si	Mn	N	P	S	O	Ni	Cu	Al	Nb	As (ppm)	B (ppm)
Conventional H13 steel	0.39	5.0	1.15	0.96	1.1	0.4	0.028	0.024	< 0.005	–	0.103	0.043	0.029	0.02	70	9
AISI H13 powder	0.4	5.4	1.3	1.2	1.3	0.5	0.03	0.011	0.011	0.03	–	–	–	–	–	–

Table 2 Manufacturing parameters and number of different specimen types for each variant

Variant	Process parameters					Number of specimens		
	Polar angle (°)	Layer rotation (°)	Laser power (mm/s)	Scan speed (W)	Surface treatment	Cube	Tensile	Fatigue
CS H13 (annealed)	–	–	–	–	–	–	5	19
CS H13 (1040 °C, 20-min, oil quenching; 3 × 570 °C tempering)	–	–	–	–	–	–	5	20
S10, 0°, high porosity, turned	0	79	500	80	turning	3	–	6 ^a
S10, 0°, low porosity, as-built	0	79	100	100	as-built	3	7	6 ^a
S10, 0°, low porosity, turned	0	79	100	100	turning	3	7	20 ^a
S3, 0°, low porosity, turned	0	79	100	100	turning	3	6	20
C3, 0°, low porosity, turned	0	79	100	100	turning	3	6	20

^aThe fatigue tests of the three S10 variants, i.e., with high and low porosities, as-built and turned surfaces, were performed at the beginning as a preliminary investigation, with six specimens for each variant. Later, for further investigation of the three different scan patterns, 20 fatigue specimens were generated for each variant

Kitagawa–Takahashi diagram to obtain more detail information of the fatigue properties.

$$\sigma_w = \frac{C_1(H_v + 120)}{(\sqrt{area})^{1/6}} \tag{4}$$

Parameter C_1 indicates the location of the critical defect and corresponds to 1.43 for surface located defect, 1.41 for defect in contact with the surface and 1.56 for volume defect, respectively. The variable defect size \sqrt{area} refers to the area of the defect. According to Murakami, for irregularly shaped defect it is determined by an effective area of a smooth contour, which covers the original irregular shape [54]. For simplicity only the pure area of the defect is applied for \sqrt{area} in this study.

For comparison, the same characterization and mechanical tests were performed on two conventional tool steel variants in two heat treatment conditions, i.e., in the annealed and hardened one.

Results

Metallographic characterization

A comparison with the microstructures from the conventionally manufactured tool steels is given in Fig. 2. The three scan patterns from the *PBF-LB/M* process display similar microstructure. Here the microstructure pictures are taken from C3 pattern. In the following if not specifically pointed out, the status of the samples displayed is of low porosity and turned surface. The conventional tool steel in the annealed state in Fig. 2a shows ferrite grains with many small spherical cementite precipitates distributed within the ferrite grains. A certain level of micro-segregation can be observed due to the uneven distribution of precipitates in the form of parallel stripes present in the cross section. After heating and quenching the steel in Fig. 2b displays an overall lath-shaped martensitic microstructure with many small spherical cementite precipitates. Additionally, macroscopically precipitated carbide segregations in

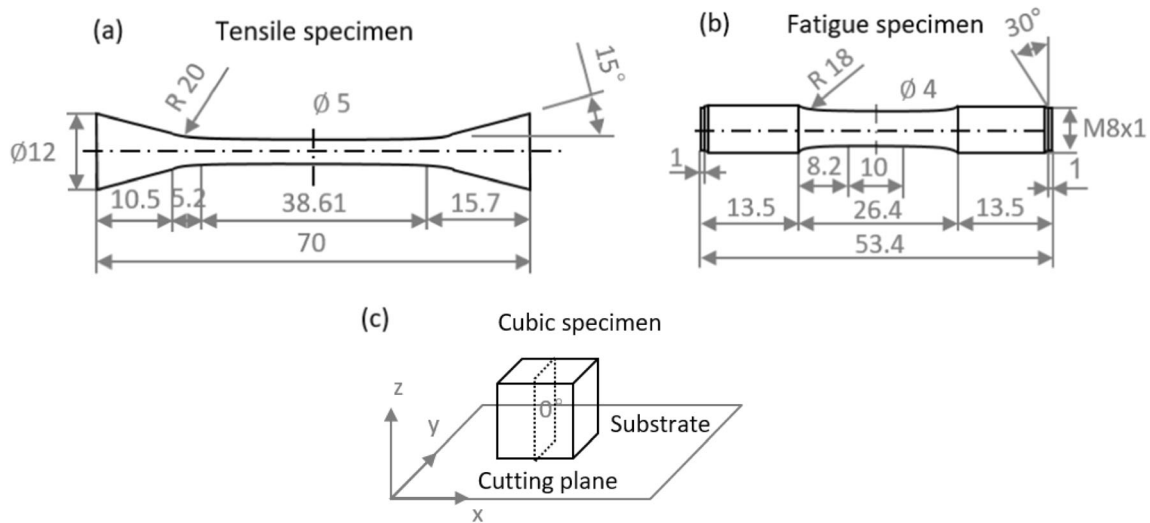


Figure 1 Geometries of **a** tensile and **b** fatigue samples, **c** orientation relationship of the cross sections of cube in regard with the metallographic investigation.

line form are visible. On a similar magnification scale, H13 processed by *PBF-LB/M* method in Fig. 2c presents a microstructure with dendrite structures with lath martensite. A vertically located crack at the cluster boundary can be observed. The microstructures taken with SEM are displayed in Fig. 2d, e and f. Similarly, compared to the microstructure of hardened conventional steel, *PFB-LB/M* fabricated H13 displays broader bundles of columnar cluster consisted of finer lath martensite growing along the building direction. The precipitates in *PBF-LB/M* H13 are finer than the ones exhibited in the conventional hardened H13. Further follow-up XRD analysis on a cubic cross section of C3 0° showed the *PBF-LB/M* fabricated H13 contains not only martensite but an amount of 20.4% retained austenite.

The metallographic results of all *PBF-LB/M* generated H13 steel variants display similar microstructures. Exemplary microstructures of H13 steel from *PBF-LB/M* are displayed in Fig. 3. Please note that the pictures of *PBF-LB/M* generated H13 in Figs. 2 and 3 were taken from different areas. In the microstructure of S10 cube at low magnification in Fig. 3a, along the building direction (z) parallel laser scanning tracks perpendicular to z direction are clearly displayed. Within these tracks some spherical pores and irregular shaped lack of fusion are visible. Also, a vertical crack and horizontal crack are observed (magnified in Fig. 3a-i and a-ii). In the magnified picture in Fig. 3b, melting pool boundaries (MPBs) of laser scan tracks are apparently visible. In Fig. 3c some

vertically aligned cracks along the columnar cluster boundaries with changing directions are present in the martensitic microstructure. WDXS distributions in Fig. 3d-i to d-iii show markings of individual element concentrations and thus segregations as fine parallel lines.

A comparison of optical micrographs of cube sections of the three scan patterns in Fig. 4 illustrates the distribution of defects with different morphologies. Each cross section is only representatively selected to present the most typical occurring defects concerning the scan pattern. The individual cross section does not represent the average defect amount for that variant; therefore, a quantity comparison is not valid. From Fig. 4a, b and c, it is evident that apart from the common spherical pores, Fig. 4c displays bigger and higher amount of horizontal elongated pores. Generally for all cube sections shown in Fig. 4d, e and f, smaller-scale vertically aligned and horizontal cracks are present. In Fig. 5 a transverse cross section of a S10 (batch 1) fatigued specimen and longitudinal sections in respect of each variant are given. The transverse section of S10 pattern in Fig. 5 displays some horizontal defects but more general spherical pores and vertical cracks. The longitudinal sections once more indicate that more spherical pores show up in S10 and S3, while horizontally elongated pores are more dominant in C3.

The porosity values obtained from the density measurements of cubes are given in Table 3. It should be noted that since the thermal history during *PBF-*

LB/M is influenced by the specimen geometry, the features obtained from cubes give a general qualitative comparisons among the different scan patterns, but not a quantitative representation of the features from fatigue specimens (as shown in Fig. 5). The measurements from the SEM pictures of the two cube cross sections of each scan strategy exhibit similar results, except for S3 with a certain obvious deviation, while the results from the Archimedes measurements of the third cube demonstrate some negative values. A negative value of porosity indicates that the density is smaller than the density at reference state, which is the state of the hardened conventional H13 steel. An explanation is given in discussion. As can be seen in Table 3, the Archimedes measurement and the examination of the SEM images lead to different results. In the image analysis, S10 shows the highest density and C3 the lowest density. In the Archimedes measurement, however, S3 shows the highest density and S10 the lowest density.

Table 4 presents the hardness results of the variants. It is apparent that the hardened CS H13 with martensite microstructure has higher hardness than in the annealed state. All *PBF-LB/M* manufactured variants display a comparable or higher hardness than the CS H13 counterparts. The average hardness measured on S10 with high porosity is lower than the other *PBF-LB/M* variants, though standard deviation indicates a non-significant difference. Among the few measured data, the points with high hardness are in the range of hardness values of the variants with low porosity. All the other *PBF-LB/M* variants exhibit similar hardness values.

The roughness values of the fatigue specimen for the as-built and turned surfaces are given in Table 5. The maximal height S_z of the as-built surface is much higher at the underside than other remaining sides. The surface with the maximal roughness value is mostly on the side of the removed support structure with some remaining structure. For the turned surface, the roughness is much lower than the as-built surface but still relatively high for a turned surface.

Tensile test

Table 6 demonstrates the tensile properties of the H13 steel. The postsurface machining process failed for S10 variant due to the high hardness and roughness; therefore, the data of S10 are not available. The tests show that the strength of the hardened conventional

steel is significantly higher than of the annealed steel, at the expense of reduced ductility. A few *PBF-LB/M* manufactured variants exhibit comparable strengths to the hardened CS H13. Most variants display generally lower strengths and ductility. All *PBF-LB/M* variants show brittle fracture with very low fracture elongation. When comparing the different scan patterns, S3 displays the best tensile properties. The strength reaches almost the strength of the hardened CS H13, while S10 with as-built *PBF-LB/M* surface displays overall lowest tensile properties.

Fatigue investigation

The SN curves obtained from the fatigue tests and the corresponding median fatigue strengths with 50% failure probability and the corresponding scatter range are illustrated in Fig. 6, with the conventional steels as reference. Table 7 displays the median fatigue strength and the scatter values, calibrated from the Weibull distribution (Eq. (2)). Figure 6a and b compares the fatigue results of S10 scan pattern with respect to different porosities and surface roughnesses. It reveals that the hardened CS H13 has higher fatigue properties than the annealed steel. The fatigue strength of S10 with low porosity and as-built surface is lower than S10 variant with high porosity and turned surface. The variant of S10 pattern with low porosity and turned surface possesses higher fatigue strength than the two variants of high porosity or as-built surface. This variant covers the fatigue range of annealed CS H13 and reaches the lower scatter range of the fatigue strengths of the hardened steel. Due to the limitation of manufacturing space, variants S10, S3 and C3 of low porosity consist of two or three batches, which were generated separately. When taking a closer look at the fatigue data for this S10 variant which consists of three batches fabricated separately in Fig. 6 c and d, the three batches hold different fatigue properties, with apparent gaps in between. The samples from batch 1 achieve significantly better fatigue properties compared to batch 2 and 3. Due to this finding in the following the three batches are analyzed separately. Batch 1 with the best possible properties reached by S10-variants is considered as representative of S10. Figure 6e and f illustrates the fatigue results from different scan pattern. It can be seen that the data of S3 lie beneath the one of C3. The fatigue strength of C3 is comparable or even a bit higher than the

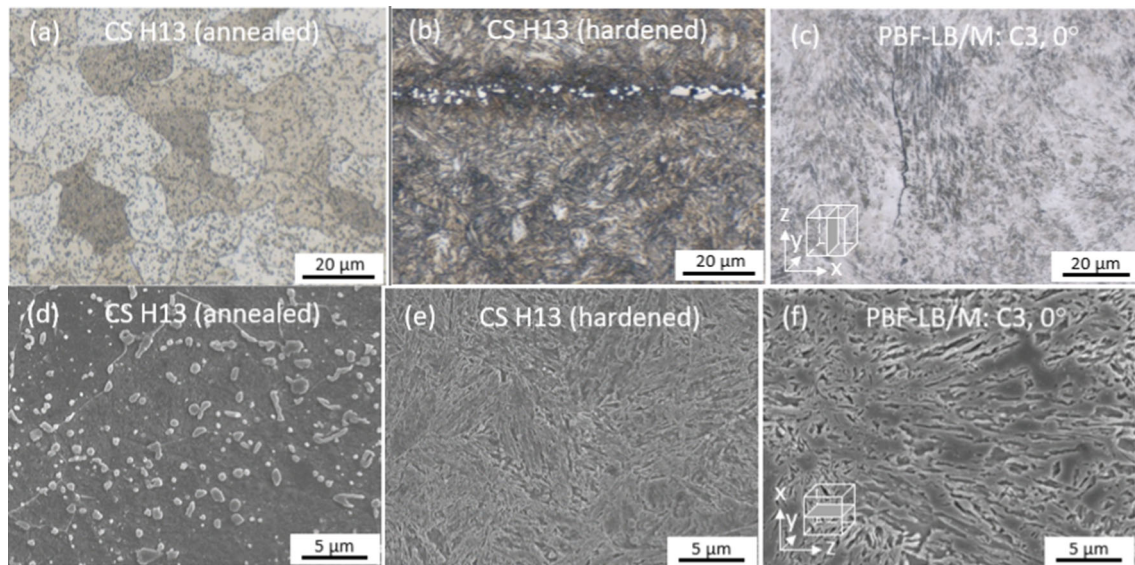


Figure 2 Comparison of exemplary metallographic microstructures of *PBF-LB/M* and conventionally generated tool steel samples under optical and scanning electron microscopes, etchant Kalling I, **a** conventional steel in annealed state, **b** conventional steel in hardened state (1040 °C, 20-min holding, oil quenching;

3 × 570 °C tempering), **c** *PBF-LB/M* processed H13 with C3 scan pattern at the melt pool scale level with *z* referring to the building direction, **d** and **e** conventional steels, respectively, in annealed and hardened states under SEM, **f** *PBF-LB/M* produced H13 (C3) under SEM with building direction *z* along the right direction.

annealed CS H13. Batch 1 of S10 displays better fatigue strength than C3.

Figure 7 demonstrates the typical fracture types of the conventional and *PBF-LB/M* manufactured tool steels. For CS H13 in the annealed state, the common fracture origins are from the surface (Fig. 7a), or from critical inclusions, mostly composed of AlSiCaMg-oxides, located in the sample (Fig. 7b). Regarding the hardened CS H13, all fractured samples failed from the surface at surface imperfections (Fig. 7c). When it comes to the *PBF-LB/M* fabricated samples, all three tested samples with high porosity failed from many big cavities present on the fracture surfaces. The exact fracture origins are not recognizable. All samples with as-built surface failed from the very rough surface on the support structure side due to incompletely removed support structure (Fig. 7d). Concerning the variants with different scan patterns, all samples failed from the characteristically featured defects brought in by the *PBF-LB/M* process—lack of fusion. There are two types of lack of fusion present here, i.e., cavity with smooth appearance or cavity with appearance with parallel lamellar lines which are, respectively, assigned as cavity and lamellar structure in the following part. Figure 7 f and g

displays the lamellar structure fracture and cavity fracture.

The sizes of the critical defects of all fractured specimens in CS H13 and all specimens of *PBF-LB/M* manufactured H13 were measured. Figure 7h visualizes the distribution of the critical defects of the different scan pattern variants on the fracture surface. The visualization is conducted according to the defect size and position, to find out their dependencies on the specimen's geometry/position. For samples labeled with the position of the support structure the photograph of the fracture surface is rotated with the side of the previous support structure to the bottom. Since most defects are of hundreds micrometers diameter some with even over thousands of micrometers, for each defect the distance to the surface can be characterized by the distance of the closest point or the gravity point of the defect to the surface. In Fig. 7h the distance of the gravity point to the surface is used. Generally, it can be derived that most defects locate close to the surface. The large cavities of S10 with extensive area coverage and a few defects from C3 lie in the volume of the specimens. Other defects of variants S3 and C3 are randomly distributed around the surface near region of the cross section, indicating no particular relation

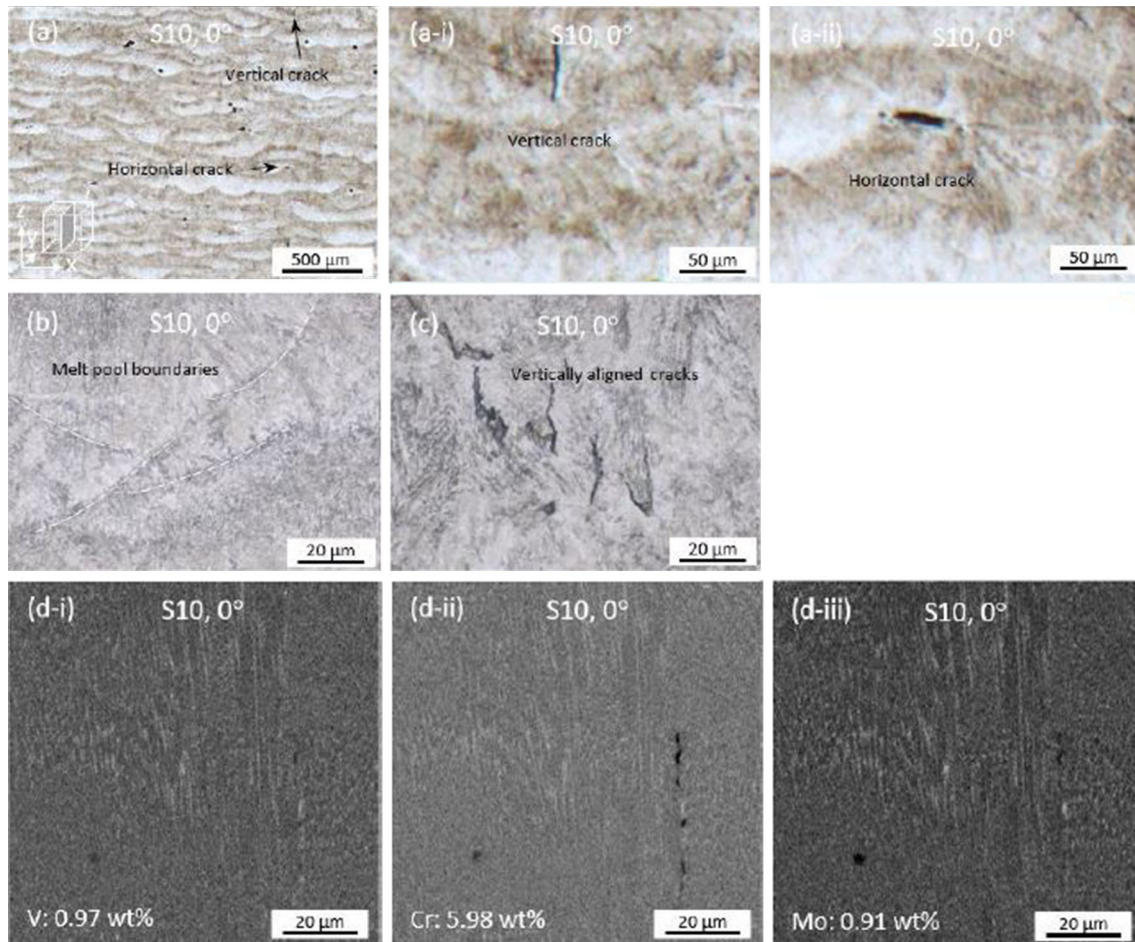


Figure 3 Exemplary metallographic microstructures of *PBF-LB/M* manufactured tool steel samples under optical and X-ray spectroscopy, **a** *PBF-LB/M* processed H13 with S10 scan pattern at low magnification with z referring to the building direction, **a-i** magnified vertical crack from **a**, **a-ii** magnified horizontal crack from **a**, **b** S10 at the melt pool scale level with elevated

magnification, **c** S10 at higher magnification presenting the details of the cracks within the microstructure, **d-i–d-iii** WDXS analyses of element V, Cr and Mo at the melt pool level with respective overall contents in weight percentage given in the pictures.

between the position of the critical defect and the defect size for the scan patterns. The defects in variant S10 with batch 2 and 3 are very large with sizes over 1000 μm , and they are mostly located in the upper part of the fracture area.

The sizes of the critical defects from different scan pattern variants are compared. Also, the surface cavity defects of which most contours are closed are analyzed. The critical inclusions present in CS H13 (Fig. 7b), especially in the annealed state, are of similar sizes ranging from 20 to 60 μm (i.e., $\sqrt{\text{area}}$ from 17 to 50 μm). This is smaller than the smallest size of critical defects present in *PBF-LB/M* generated H13 given in Fig. 8. Figure 8a shows the Fréchet size distributions (Eq. (3)) of the overall critical defects

with respect to the different scan patterns. It can be derived that S3 has the smallest critical defect sizes, while the S10, consisting of three batches, holds the largest critical defect sizes. When analyzing the critical defects of the three batches separately, S10 batch 1 possesses a medium range of defect sizes in between S3 and C3 variants; S10 batch 2 and 3 show significantly larger critical defect sizes. Further separated evaluations of respective critical cavity and lamellar structure, with the overlap of the mixed defects, are presented in Fig. 8b. S10 batch 2 with one lamellar structure and one cavity failures, and S10 batch 3 with all cavity failures are not considered. The three distributions of cavities, lamellar structures and the defect mixture of each scan pattern are

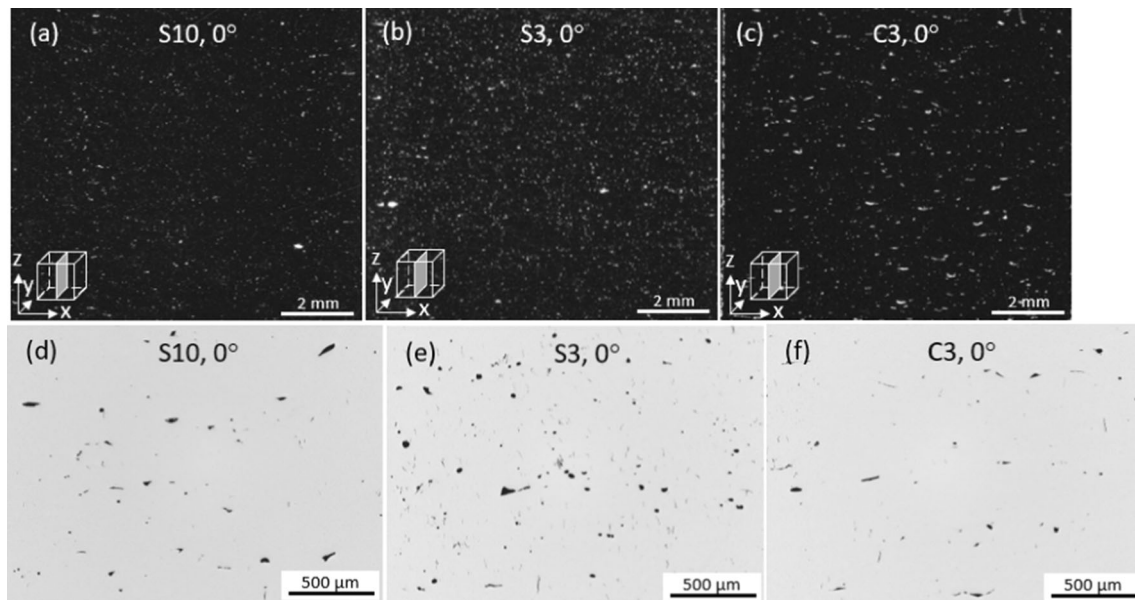


Figure 4 Metallographic investigation of defects in cube cuts at different orientations, **a**, **b** and **c** overview of the cube cut of pattern S10, S3 and C3, **d**, **e** and **f** corresponding magnified views.

separately displayed in the inset in the diagram. It can be seen that for all three scan patterns, cavity and lamellar structure follow the same distribution trend as the mixture of the defects. S10 batch 1 has comparable defect sizes as S3, while C3 exhibits largest distribution sizes. The defect size is in an increasing order from S3, S10 batch 1 to C3. Furthermore, the detailed distribution parameters for the Fréchet equation (Eq. (3)) are given in Table 8.

The Kitagawa–Takahashi diagram with the fatigue strength predicted by Murakami (reference to Eq. (4)) is given in Fig. 9. All variants show very similar hardness; therefore, the predicted fatigue strengths are almost the same as exhibited by the solid lines in the diagrams. In an ideal condition where Murakami's formula depicts the fatigue properties of the *PBF-LB/M* generated tool steels well, the Murakami's fatigue strength would be the border line between the run out and fractured samples, separating the run out samples in the area below and the fractured samples above the line. It is apparent from the diagram that Murakami's equation overestimates the fatigue strength for all variants. The relative positions of the data range of each variant give rough comparisons of the fatigue strengths among the different variants. When referring to the run outs, at similar defect sizes, C3 has run outs at higher stress levels than S3 and S10 batch 3. At the same stress amplitude one run out of C3 shows a slightly smaller defect size than the only

run out from S10 batch 1. This indicates that the fatigue strength: S10 batch 1 > C3 ≥ S10 > S3. Furthermore, the defect size ranges of S3 and S10 batch 1 are similar approximately from 100 to 300 μm, whereas C3 has a larger defect size range from around 100 to 500 μm.

Discussion

General comparison of fatigue strengths between conventional and *PBF-LB/M* steels

The fatigue investigation of a variety of *PBF-LB/M* generated H13 steels with multiple varying features reveals numerous impact factors on the fatigue properties, with the conventional steels as references. The fatigue strength of the hardened CS H13 is higher than the annealed CS H13 as a result of the higher hardness and the respective microstructure. From Fig. 2e and f the martensite microstructure looks coarser in *PBF-LB/M* variants than the hardened CS H13. However, owing to the formation of cluster domains and sub-grains within each domain in *PBF-LB/M* process, the martensitic lath is finer in *PBF-LB/M* variants like stated by several authors [36, 55]. Compared to the *PBF-LB/M* fabricated H13 variants the hardened CS H13 has highest fatigue properties, like concluded by Mazur [35], Garcias [50], Pellizzari

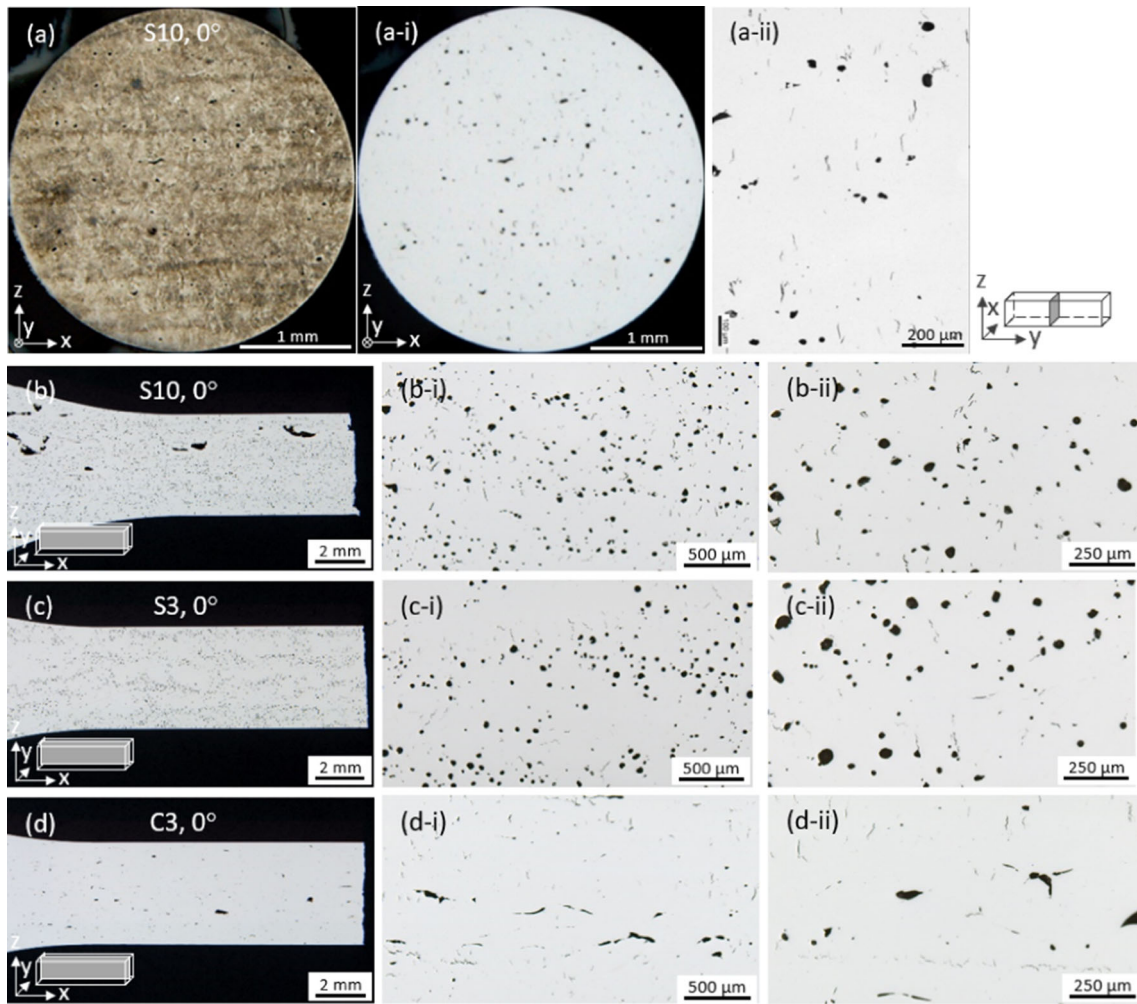


Figure 5 Metallographic investigation of a transverse cross section of a fatigued specimen from S10 batch 1 and longitudinal cross sections from each variant at different magnifications, **a** cross section S10, **b** longitudinal section S10, **c** longitudinal section S3, **d** longitudinal section C3.

Table 3 Porosities of PBF-LB-M generated cube samples

Variant	SEM of cube 1 (%)	SEM of cube 2 (%)	Average SEM (%)	Archimedes of cube 3 (%)
CS H13 (annealed)	–	–	–	0
CS H13 (hardened)	–	–	–	0
S10, 0°, high porosity ^a	–	–	–	6.14
S10, 0°, low porosity ^b	0.59	0.47	0.53 ± 0.08	– 0.30
S3, 0°, low porosity ^b	0.33	1.21	0.77 ± 0.62	– 1.63
C3, 0°, low porosity ^b	0.91	0.79	0.85 ± 0.08	– 0.78

^acube of S10, 0°, high porosity was produced separately for a first preliminary investigation on the influence of laser power and scan speed on the porosity; ^bcubes of S10, S3 and C3, 0° with low porosity were produced later in another batch together for further insight on the influence of scan pattern on porosity

[51], Macek [52] and Dörfert [53] et al. The metallographic analysis of the H13 samples processed by PBF-LB/M presents a high amount of cracks as also

described by Qin et al. [26] and other researchers [55, 56]. In Fig. 3a and c vertical and vertical aligned cracks are observed which can be assigned to hot and

Table 4 Hardness values of *PBF-LB/M* generated cube samples

Variant	Hardness [HV1]	Measured points
CS H13 (annealed)	206 ± 7	13
CS H13 (hardened)	528 ± 6	29
S10, 0°, high porosity	525 ± 110	7
S10, 0°, low porosity	568 ± 17	100
S3, 0°, low porosity	579 ± 15	100
C3, 0°, low porosity	571 ± 15	100

Table 5 Roughness of *PBF-LB/M* generated fatigue sample

H13	As-built surface		Turned
	Remaining side	Underside	
S_z (μm)	341 ± 71	593 ± 131	77 ± 36

solidification cracks [4]. According to many researchers, the plenty of small and sharp cracks and pores in the microstructure [50, 52, 54], the bigger size of the critical lack of fusion defects [50, 54] and residual stresses [35] all together play an important role in the deteriorated fatigue properties of H13 produced by *PBF-LB/M*. The further investigated fracture surfaces indicate that all specimens of the *PBF-LB/M* generated steel failed from typical lack of fusion defects [51] located either at the surface or within the sample [50–52] as described by Pellizarri et al. and other researchers. The lack of fusion defects comprised of cavity and lamellar structure. The sizes of the lack of fusion defects in *PBF-LB/M* steels are much bigger than the sizes of the inclusions in the annealed CS H13 [50, 52]. Different to many other research work reporting generally inferior fatigue

strength of *PBF-LB/M* generated H13, the fatigue properties of S10 batch 1 come close to the values of the hardened CS H13. According to Murakami [54], this can be partly attributed to the improved hardness, compensating the disadvantages of the bigger and irregular defects present. Additionally the finer microstructure might play a role.

Comparison of fatigue strengths of *PBF-LB/M* steel with respect to roughness and porosity

When considering the multiple influencing factors among the *PBF-LB/M* variants, for the S10 pattern with as-built *PBF-LB/M* surface, all samples failed from the underside of the removed support structure, where the roughness is much higher than on the remaining surface. The still high surface roughness on the remaining surface results from balling effects due to unstable melted scan tracks [57, 58] and from some incompletely melted or extra particles adhered to the surface [59]. The higher roughness with the maximal height S_z on the underside is caused by the incompletely removed support structure, which is more severe than the intrinsic surface roughness brought by the *PBF-LB/M* process and is the main reason for the crack initiation. In comparison with the S10 with high or low porosities and with different surface roughness, the fatigue properties are lowered in that case more significantly by the increasing level of roughness than the level of porosity. It was reported that crack initiation tends to take place at cavities near the surface rather than at bigger cavities in the center of the specimen, which infers that failures at the surface lead earlier to failure than failures in the volume [54]. It is further reported that

Table 6 Tensile properties of *PFB* generated tool steel samples

Variant	Young's modulus (GPa)	Yield strength (MPa)	Tensile strength (MPa)	Fracture elongation (%)
CS H13 (annealed)	195 ± 14	345 ± 7	619 ± 2	28.8 ± 1.2
CS H13 (hardened)	211 ± 1	1431 ± 17	1707 ± 16	7.5 ± 0.2
S10, 0°, low porosity, as-built surface	181 ± 26	829 ± 38	956 ± 82	0.5 ± 0.4
S10, 0°, low porosity, turned surface	Postmachining processing failed			
S3, 0°, low porosity, turned surface	194 ± 5	1213 ± 22	1630 ± 41	1.6 ± 0.2
C3, 0°, low porosity, turned surface	198 ± 6	893 ± 54	1440 ± 35	1.5 ± 0.3

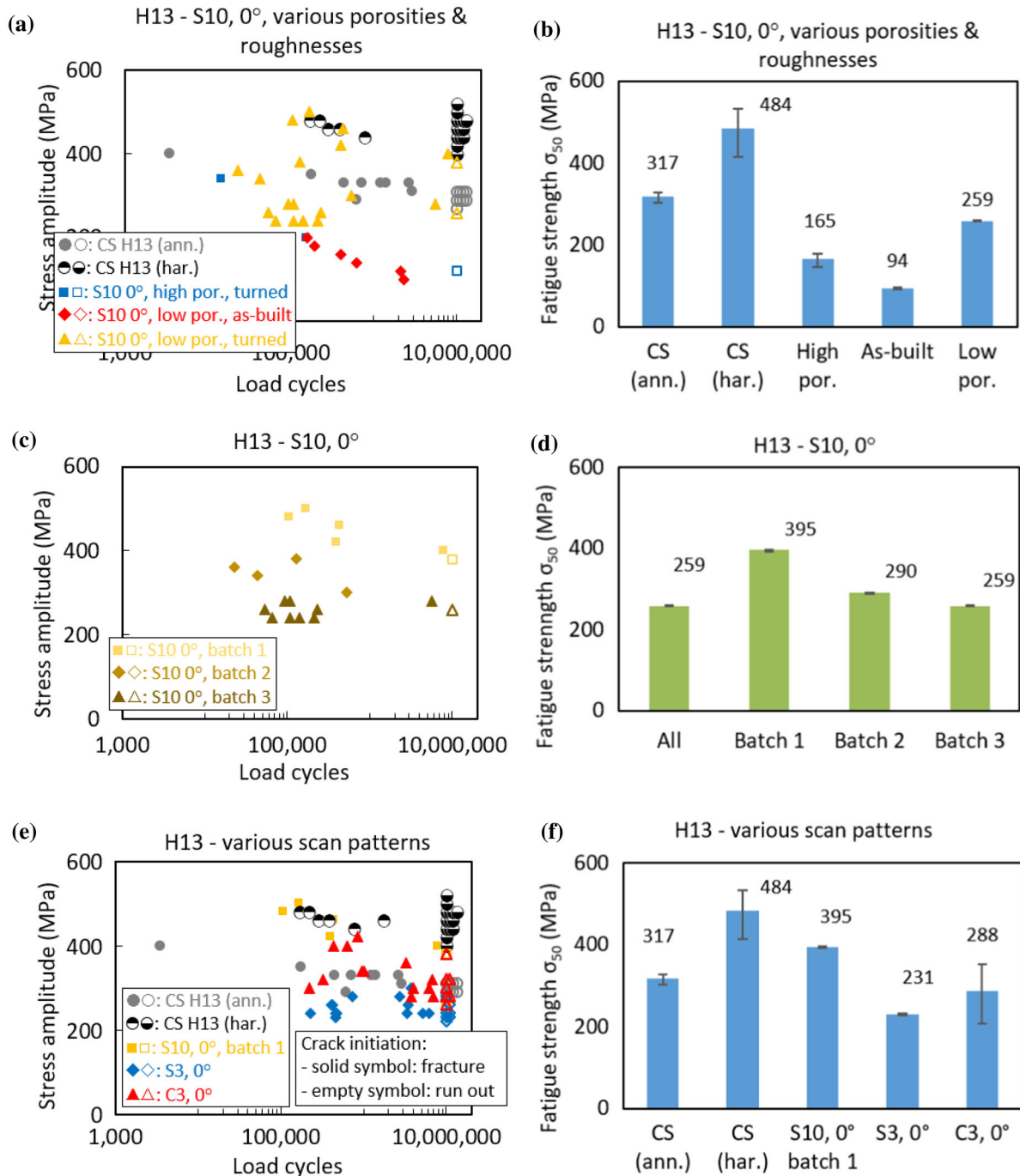


Figure 6 S–N curves and histograms of median fatigue strengths of PBF-LB/M generated tool steel samples, **a** and **b** overall combined S–N data and fatigue strength diagram of three S10 variants with features of high porosity with turned surface, low porosity with as-built PBF-LB/M surface, low porosity with turned

compared to the turned samples with consequent compressive residual stresses, tensile residual stresses usually arise at the as-built surfaces [60], with detrimental effect to the fatigue behavior [35]. The

surface; **c** and **d** individual S–N data and fatigue strength diagram of S10 containing three different batches; **e** and **f** overall combined S–N data and fatigue strength diagram with scan patterns of S10, S3, C3.

adverse influence of the roughness with a maximal height S_z of 593 μm here and with an overlapped impact of tensile residual surface stresses prevails the negative effect from the high porosity of 6.14%. With

Table 7 Fatigue limits with 10%, 50% and 90% fracture probabilities and the corresponding shape parameters of Weibull distribution (Eq. (2))

Variant	σ_{10} (MPa)	σ_{50} (MPa)	σ_{90} (MPa)	m
CS H13 (annealed)	303	317	327	42
CS H13 (hardened)	415	484	533	12
S10, 0°, high porosity, turned surface	181	186	190	62
S10, 0°, low porosity, as-built surface	91	94	96	51
S10, 0°, low porosity, turned surface—batch 1, 2 and 3	257	259	261	194
S10, 0°, low porosity, turned surface—batch 1	391	395	397	195
S10, 0°, low porosity, turned surface—batch 2	287	290	292	194
S10, 0°, low porosity, turned surface—batch 3	257	259	261	194
S3, 0°, low porosity, turned surface	228	231	232	185
C3, 0°, low porosity, turned surface	209	288	352	6

an increased level of porosity or a slightly lower level of roughness, the inferior impact of the roughness and the porosity is identical.

Comparison of fatigue strengths of PBF-LB/M steel with regard to scan pattern

Based on the current results, the trend among the various scan patterns shows that the fatigue strength is highest in S10 batch 1 with intermediate sizes of critical defects, while S3 has the lowest fatigue strength with the smallest critical defects. Variant C3 shows intermediate fatigue strength but with largest critical defects. The incompatible trend between the fatigue strength and critical defect size indicates that apart from the largest defect the fatigue strength is impacted by other factors. The results concerning fatigue properties imply the scan patterns influence the fatigue behaviors in different ways. However, based on the micrographs, there are no obvious features that explain why variant S3 has the worst fatigue properties.

Coming to the variants with the lowest porosity of various scan patterns, different to the generally scattered fatigue test results due to the statistical distribution of the defects in the work of Pellizzari et al. [51], the fatigue strength distributions of variants S10 and S3 exhibit excessively high values of the shape parameter m whose highest value reaches almost 200 (Table 7). The high m value refers by definition to a steep slope of the fatigue limit distribution. It is because of lack of run out samples, especially for the case of S10. Therefore more fatigue test data in the level of the fatigue strength are demanded for more reliable fatigue strength statements.

Critical defect and its geometry dependence with regard to size and position

The distinct size distributions of the largest defects can be related to the formation mechanism of lack of fusion defects in PBF-LB/M process. Wu et al. found the lack of fusion is preferably located between the individual melting pools [4], and thus, the interfaces between the scan tracks or scan layers are usually the common sites for the formation of the larger stretched lack of fusion defects. As a result, for the different scan patterns, C3 with smaller scan vector and separate chessboard pattern generates more interfacial scan tracks, thus a higher possibility of formation of the larger lack of fusion defects. From Fig. 4 and Fig. 5 it can be derived that the lack of fusion is larger in C3 than S3 pattern, while lack of fusion is also bigger than hot and solidification cracks. Accordingly, it has a higher potential of forming larger sizes of the largest lack of fusion defects and therefore higher size range than S3 and S10. However, S3 has the smallest critical defects, which can be attributed to its steepest temperature gradient as explained as follows. Compared to S10, S3 has a shorter track length and closer distance between the turning points, and it spends more exposure time within a smaller area. This results in a more even distribution of laser energy within the same area, and therefore, the energy input and local temperature are higher. Hence the temperature gradients are steeper in the S3. Similarly, C3 with separate scan sequence of small tile areas leads to a temperature gradient lying between S3 and S10. The energy input and temperature gradients are therefore $S3 > C3 > S10$. Based on the different forming mechanisms, hot cracks in the center of melt pool are caused by very high energy input [4]. Solidification cracks between neighboring

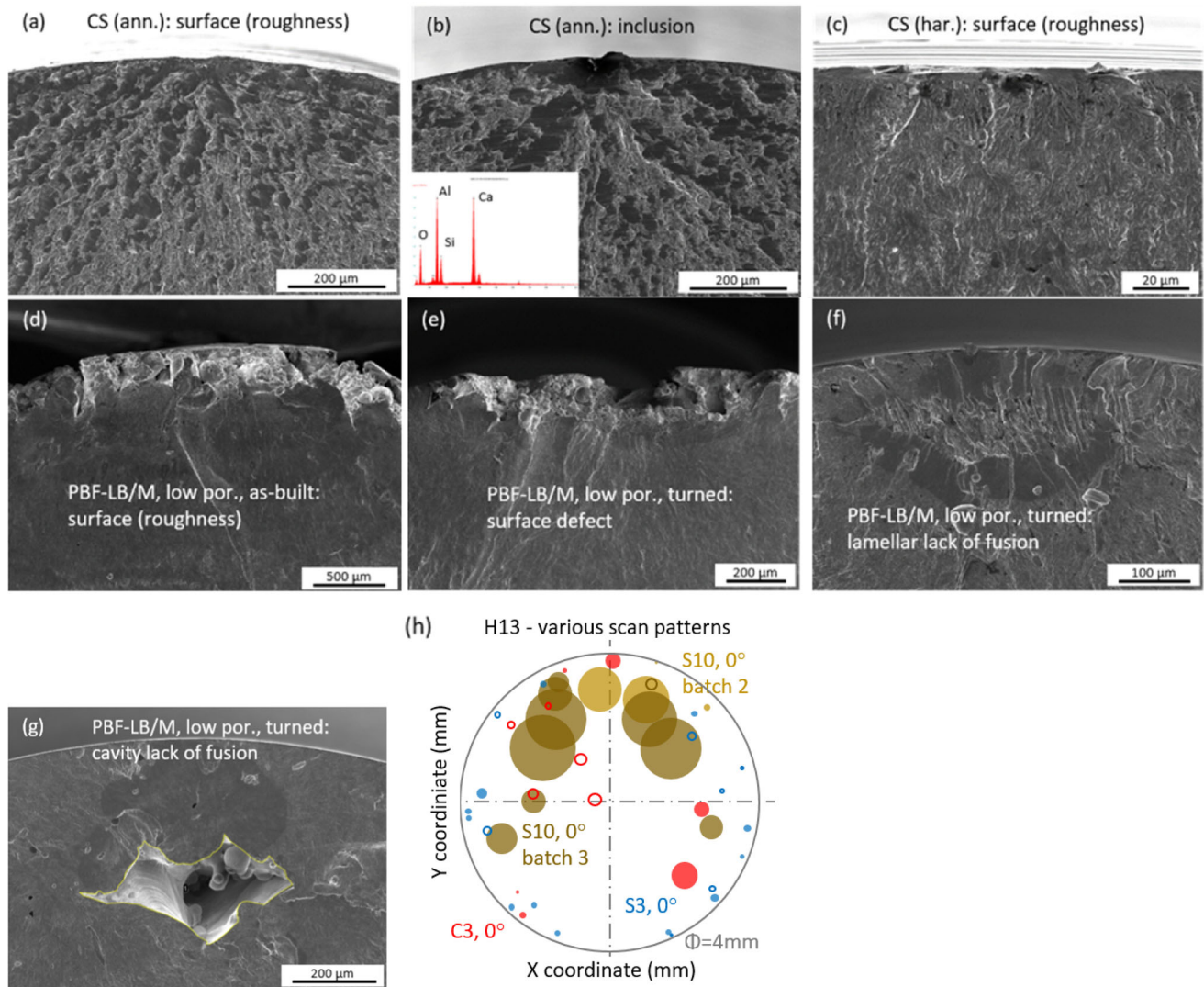


Figure 7 Typical SEM pictures of the fracture types of conventionally and *PBF-LB/M* generated tool steel fatigue samples as well as the critical defect distributions according to the positions of the gravity centers on the fracture surfaces including the position and size information, **a** surface (roughness) initiating fracture from CS H13 sample at annealed state, **b** inclusion initiating fracture from CS H13 sample at annealed state with inset of the corresponding EDX analysis of the inclusion, **c** surface (roughness) initiating fracture from CS H13

sample at hardened state, **d** surface initiating fracture from *PBF-LB/M* sample in as-built condition, **e** surface (defect) initiating fracture from *PBF-LB/M* sample with turned surface, **f** lamellar structure initiating fracture from *PBF-LB/M* sample, **g** cavity initiating fracture from *PBF-LB/M* sample, with the cavity contour outlined referring to the defect area, **h** position and size distributions of the critical defect in S10, S3 and C3, the circle diameters are proportional to the defect sizes, which, however, are not correlated to the size of the specimen cross section.

clusters are induced by the element segregation degree [4, 29]. Lack of fusions between scan tracks and deposited layers is triggered by lack of energy input [4, 61]. As a result, hot and solidification cracks are smaller than lack of fusion (Figs. 4 and 5). The highest temperature gradient and energy input in S3 promote formation of hot cracks and solidification cracks [25, 62]. Accordingly, the potential of forming smaller sizes of critical defects is also highest in S3. In

short, the scan patterns yield various thermal histories creating diverse forms of the critical defects.

The further size and position dependencies of the critical defects on the geometry of the specimen are only revealed in the variant S10 batch 2 and 3, whose largest defects are located in the upper half region on the fracture surfaces of the specimens (Fig. 7h). The reason for these dependencies is probably owing to different thermal histories and needs further

Figure 8 Overall and respective critical defect size distributions of PBF-LB/M generated tool steel samples, **a** overall defect size distributions with scan patterns of S10, S3, C3; the distribution of S10 which contains three batches with inconsistent properties is further separated into three defect size distribution of the respect batch; **b** separate cavity and lamellar structure size distributions and overall defect size distributions of S10, S3, C3; the distribution of S10 is represented by batch 1 with the best properties.

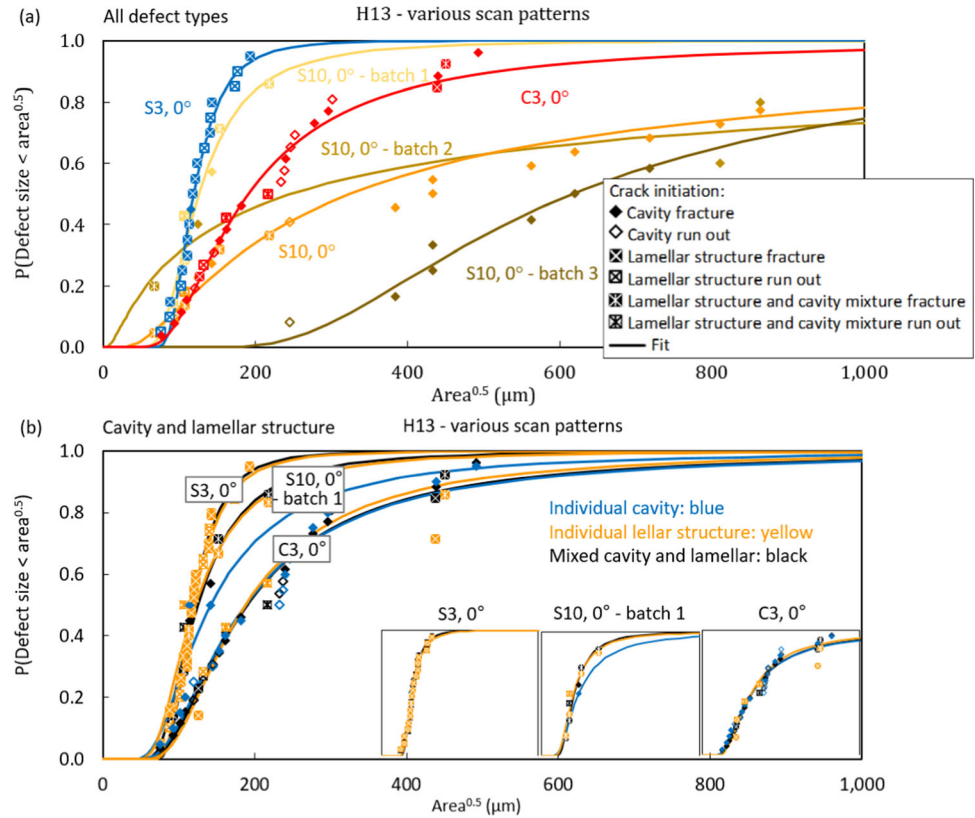
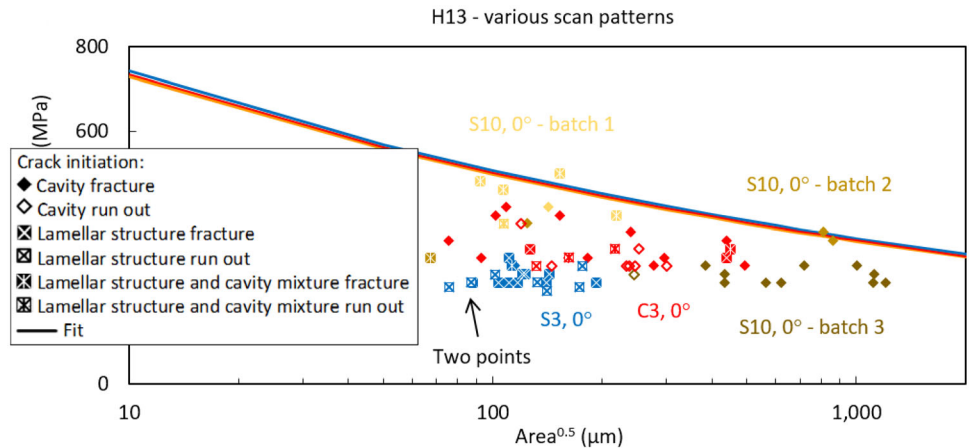


Table 8 Overall and individual defect size distribution parameters of Fréchet equation (Eq. (3))

Variant (low porosity, turned)	Overall defect		Cavity		Lamellar structure	
	$d_{m, all}$ (μm)	c_{all}	$d_{m, cav}$ (μm)	c_{cav}	$d_{m, lam}$ (μm)	c_{lam}
S10, 0°—batch 1, 2 and 3	324	0.9	574	1.6	111	2.3
S10, 0°—batch 1	125	2.9	142	2.0	122	2.6
S10, 0°—batch 2	247	0.6	423	0.6	67	0.8
S10, 0°—batch 3	617	1.8	617	1.8	—	—
S3, 0°	119	4.7	115	0.8	119	4.3
C3, 0°	191	1.9	188	1.8	188	2.0

Figure 9 Kitagawa–Takahashi diagrams of PBF generated tool steel samples with parameters from Murakami formula.



investigations. Furthermore, H13 displays many crack initiations occurring in the volume. The underlying reason can be owed to the residual stresses introduced by the *PBF-LB/M* process. The residual stresses in H13 can reach the magnitude of its yield stress, which is almost 1500 MPa [35, 36]. The high surface tensile residual stresses in as-printed H13 can be turned into compressive state due to turning and increase the balancing tensile stresses within the volume. This promotes crack initiations in the volume.

Matrix strength

The prediction offered by the Kitagawa–Takahashi diagram (Fig. 9) was not expected to be accurate, since the fatigue strength predicted by Murakami formula is valid for symmetric loadings and spherical critical defects only, while the critical defects present in *PBF-LB/M* H13 steel are commonly elliptical or of irregular shapes. If an elliptical defect is very elongated, the predicted fatigue strength is overestimated, due to a higher stress intensity at the elongated defect. Here this difference is neglected.

Except for S10 batch 1, all fatigue results lie below the fatigue strengths predicted with the Murakami-Eq. (4). This exhibits a weakened strength of matrix compared to the CS H13. Regardless of the higher hardness of *PBF-LB/M* variants, the weaker matrix strength is probably related to other microstructural factors. The chemical composition in Table 1 exhibits that the nitrogen content is higher in the *PBF-LB/M* powder. Dörfert et al. illustrated in his work that the oxygen content is significantly higher in the *PBF-LB/M* variants than in the CS H13 [53]. He attributed oxygen and nitrogen as the reason of the weaker matrix strength in the *PBF-LB/M* variants [53]. Additionally, the weakened matrix strength can also result from a weaker metallurgical connection between the scanned layers, what could be ruled out for horizontally generated fatigue specimens. Furthermore, the deteriorated matrix strength can simultaneously result from the characteristic microstructural vertical and horizontal cracks. In the building system coordinates, lack of fusions locate horizontally, whereas hot and solidification cracks always appear in vertical or vertically aligned form. On the one hand, if the rotation of each scanning layer is neglected, the horizontal lack of fusions have almost no impact on the horizontally built fatigue

specimens. However, due to the rotation of each layer, the lack of fusions are not always necessarily parallel distributed to the sample loading axis and therefore can decrease the matrix strength for the horizontal specimens to a certain limited extent. On the other hand, because of the vertically aligned orientations and higher amounts of hot and solidification cracks, they are taken as the decisive deterioration factors for the matrix strength, despite the smaller sizes as compared to the horizontal lack of fusions.

For the different scan patterns, S3 has the lowest matrix strength because of its higher possibility of forming solidification and hot cracks. Accordingly, although C3 possesses the highest amount and biggest sizes of lack of fusions, the possibility of forming solidification cracks lies between S3 and S10, i.e., $S3 > C3 > S10$, which in turn reduces the corresponding matrix strength, i.e., $S3 < C3 < S10$. This can be confirmed by the relative distance of the data points of each variant to the respective Murakami predicted strength, i.e., $S3 > C3 > S10$ batch 1.

Superimposed effects of critical defect and matrix strength on fatigue strength

The findings of the matrix strengths among the various scan patterns are in the same trend as the discoveries of the fatigue strengths, which indicate that not only the largest defect size but also the matrix strength plays an important role in the fatigue properties. The consistent orders of the fatigue and matrix strengths differ with the sequence of the largest defect sizes, with conflicts mainly focus on C3 and S3. Referring to the final outcomes of the fatigue strengths, i.e., $C3 > S3$, it can be inferred that in this work the impact of the matrix strengths, i.e., $C3 > S3$, prevails the effect of the critical defect sizes, i.e., $C3 > S3$.

Also, the expansion of the Murakami equation ($\sigma_w = \frac{C_1(C_2+H_v)}{(\sqrt{area})^{C_3}}$) was used to show the test results better. Owing to lack of run outs thus unbalanced survival to fracture ratio and the high scatter, for some variants no reasonable values are obtained simultaneously for C_1 , C_2 and C_3 . At the same time the hardness and lack of fusion failure type are same for all *PBF-LB/M* variants, which imply the same effect from C_2 and C_3 . For this purpose the parameter C_1 in this extended fatigue strength formula is fitted

(Table 9). Since only S10 batch 3 and C3 have small percentage of surface defect failure, the calibrated C_1 is mainly suitable for the case with critical defects located within the volume. With the fitted parameter, it is possible to see the difference in fatigue properties between each variant (Fig. 10b and c).

Generally within the range of the available critical defect sizes present on the fracture surface, the difference in fatigue strength is approximate 100 MPa for variants with the various scan patterns or 100 to 200 MPa when S10 batch 2 and 3 are excluded. Accordingly, from Fig. 10 b it can be deduced that the negative impact from the larger critical defect sizes is overwhelmed by the positive effect from the higher matrix strength in C3, while it is the other way around for S3. Thus, the relation between the fatigue properties of C3 and S3 can be understood. Furthermore, from the number of samples failed at each type, it can be derived that for variants S10 batch 1, S3 and C3, the run out samples display a higher ratio of lamellar structure failure to cavity fracture than the failed samples. For S10 batch 2 and 3 with worse fatigue properties than batch 1, most samples failed from cavities. S10 batch 2 with one lamellar structure fracture displays slightly better fatigue strengths than batch 3 with all cavity fractures. Despite the similar size distributions between cavity and lamellar structure shown in Fig. 8b, combining the matrix influence, it can be inferred that cavity lack of fusion seems to be more detrimental to the fatigue properties.

In summary, it can be concluded that the fatigue properties are combined results of the largest defect sizes and the matrix strength.

Other factors diversifying fatigue strengths of conventional and PBF-LB/M steels

Furthermore, the similar matrix strength of S10 batch 1 to the hardened CS H13, on one side, comes from the higher hardness, as indicated by the absolute position of the theoretical Murakami fatigue strength in the Kitagawa diagram. On the other side it results from other beneficial microstructural factors such as finer microstructure, as implied by the relative distance of the data points to the corresponding predicted fatigue strength, etc. In contrast to the findings in our study, other work reported generally significantly lower fatigue strengths of PBF-LB/M H13 than the CS H13. In the previous co-work with Dörfert

et al. [53], it was also assumed that the gap between the conventional fatigue value and PBF-LB/M value cannot be closed, since the load capacity of the matrix of the investigated scan pattern C3 with turned surface was found to be lower. In Pellizzari's work he attributed [51] the inferior fatigue properties to the defect size distribution (size, location and orientation) and regarded hardness with marginal influence. He has not considered the influence from the matrix strength, which is in turn also influenced by the defects, hardness and so on. The hardened CS H13-similar matrix strength, as shown in our study, facilitates the achievable strength level to the conventional range; however, the existence of the lack of fusion defects prevents the further accomplishable level of the fatigue strength. Significant improvement in fatigue behaviors can only be achieved by minimizing the number and the size of the defects [51]. At the same time, the other further underlying factors still need to be found out.

Comparison of porosities in respect of scan pattern

The negative values obtained from the Archimedes density measurements are attributed to some amount of retained austenite preserved during martensite transformation in the PBF-LB/M process. By the follow-on phase measurement on the C3 cube with XRD a high amount of 20.4% retained austenite was confirmed. As is known that the density of the CS H13 with a martensitic phase ranges from 7.75 g/cm³ [56], 7.78 g/cm³ [63] to 7.8 g/cm³ [64], while conventional 316L steel of an austenitic phase is usually in the range from 7.95 [65] to 8.0 g/cm³ [66], which is higher than the density range of CS H13. It can be inferred that the face-centered cube crystal structure of austenite leads to higher packing density than the body-centered tetragonal structure of martensite; therefore, CS 316L has higher density than CS H13. An increasing amount of retained austenite will make up the density loss brought in by the pores and even exceed the density of the hardened conventional steel. Hence the negative results are a combined effect of the amount of the retained austenite and the porosity. Within this research the corresponding densities obtained for CS H13 is 7.63 g/cm³ and 7.93 g/cm³ for CS 316L. With a retained austenite content of 20.4%, calculations with a porosity value of -0.8% are obtained. Also, higher density of PBF-LB/M

H13 than the CS H13 of around 8.0 g/cm^3 was reported by some *PBF-LB/M* manufacturers [67]. It needs to be noted that the determination of austenite phase fraction using Archimedes is not reported in other literature so far; however, both the evaluation and measurement methods were properly conducted under the circumstance of this study. The roughly estimated value is also within a reasonable range. Moreover, different density values of austenite [68, 69], ferrite [69], bainite [68] and martensite [68] were reported. Similar evaluation of bainitic steel density with regard to different phase fractions of ferrite and cementite was also performed [70], where the effect of microstructures and phases on the steel density is emphasized. Because of the diverse thermal histories the amount of retained austenite is a local variable. With locally varying amounts of the austenite a comparison of porosity among the variants by the Archimedes method is not possible. From the cross section scanning the porosity of C3 is higher than S10. The porosity relation between S10 and S3 is not known, due to the high deviation between the two cross sections from S3.

Comparison of hardness concerning scan pattern

The hardness of the *PBF-LB/M* variants with different scan patterns of the lowest porosity is almost of no difference, which is about 50 HV1 higher than CS H13 in the hardened state. The higher hardness of *PBF-LB/M* steels is probably due to the fast melting and solidification speed within the *PBF-LB/M* process. This leads to finer austenitic grains thus finer martensite microstructure. At the same time the *PBF-LB/M* variant with high porosity of 6.14% holds a

Table 9 Individually and commonly calibrated parameters of each variant with parameters from Murakami as reference

Variant (low porosity, turned)	C_1	C_2	C_3
Murakami	1.56	120	1/6
S10, 0° —batch 1, 2 and 3	0.95		
S10, 0° —batch 1	1.32		
S10, 0° —batch 2	0.87		
S10, 0° —batch 3	0.96		
S3, 0°	0.78		
C3, 0°	1.04		
All variants	0.91		

lower average hardness. The highest values in this distribution are in the range of the values of the other *PBF-LB/M* variants, which implies that the lower values are influenced by pores in the matrix. This infers that within a certain extent the process parameters like laser power and scan speed have a main influence on porosity level, but the generated microstructures show no principle difference.

Tensile strength and correlation with density

The static mechanical properties of *PBF-LB/M* processed H13 under uniaxial tensile test are featured with comparable strength and remarkably lower fracture elongation of less than 2% consistent to the statement of Garcias et al. [50] compared to the CS H13. The ultra-brittleness and the existence of randomly distributed pores or cracks promote an earlier fracture and lead to the lower strengths like also stated by Bajaj et al. [5]. Furthermore, the segregations of heavy elements at the martensite grain boundaries, and the formation of precipitations can also be the reason for the inferior ductility of *PBF-LB/M* manufactured H13 [5]. A direction comparison of the influences of the scan patterns on the tensile properties is not possible in this study due to the failure in postsurface processing of the S10 variant. The generally lower strengths, especially the tensile strength of S10 with as-built *PBF-LB/M* surface compared to S3 and C3, indicate the notch effect from the rough surface. Qu et al. have classified the different plasticity and strength changes of ductile crystalline metals, conventional brittle materials and metallic glasses when a notch is introduced [71]. Both ductile crystalline metals and conventional brittle materials like ceramics showed a decreased plasticity, due to the constrained plasticity in the notch area of the ductile metals or stress concentration in the brittle materials, except metallic glasses which showed an increased fracture elongation owing to the enhanced shear band zone. With the joint negative impact of tensile surface residual stress in S10 with as-built *PBF-LB/M* surface an earlier onset of cracking is promoted, hence an earlier brittle failure of the specimen without reaching higher tensile strength. Since the brittle specimens ruptured at the highest point, the tensile strength increases with the elongation. The delayed fracture of S3 variant directs it to higher fracture elongation and tensile strength.

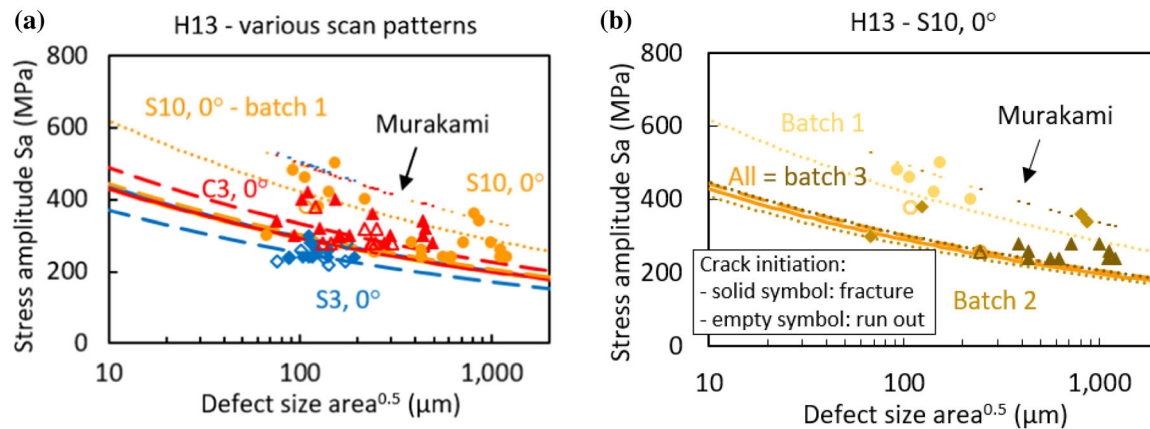


Figure 10 Kitagawa–Takahashi diagrams of calculated fatigue strength with fitted C_1 parameter from Murakami formula (Eq. (4)). The dashed lines correspond to the individually

Considering the relation between the tensile properties with porosity, generally for ductile materials, cavities act as free surfaces with no obstacles for dislocation movements. This can relieve the stress concentration to some extent. However, the facilitated dislocation movements in ductile materials in turn accelerate the propagation of the crack tip. In this way cavities are considered as cracks [72] and function as the front of crack propagation during loading or stress concentration sites. For brittle materials, the local stresses at the pore edge can not be relieved by plastic deformation [72] or stress concentration sites. For the various scan patterns, variant S3 carries better tensile properties than C3 than S10 with as-built *PBF-LB/M* surface, while the porosity of C3 is higher than S10 and S3, with the sequence of the largest pore sizes bigger in C3 than S10 than S3. A direct relation between the general porosity (or the largest pores) and the tensile properties cannot be obtained. Owing to the fact that the qualitative porosity comparison was made on cubic samples, which may quantitatively differ from the exact porosity value of the tensile or fatigue samples due to the geometry influence, further work which conduct investigations directly on tensile or fatigue samples is suggested. The mechanical behavior of the *PBF-LB/M* tool steels is a result of joint effects of porosity [50, 52], largest pores [52], residual stress [35, 50] and matrix strength of the microstructure [72, 73].

calibrated C_1 parameter for each variant, and solid lines correspond to the commonly calibrated C_1 parameter for all variants.

Correlation of fatigue strength with density

The pores are considered as existing cracks for the fatigue behavior with mathematical relationship between the largest pore size and the fatigue strength. Due to the mixed contribution of the matrix strength and the largest pore to the fatigue strength, a simple single relation between the porosity and the fatigue strength does not exist. Macek and Garcias et al. have addressed in their works the effect of porosity on fatigue response [50, 52]. Under the same stress amplitude, higher porosity in the specimen promotes an earlier fatigue fracture, despite the negative influence from larger pore sizes or closer-to-surface distance. Additionally, the pore size can also be a relevant parameter estimating the trend of the fatigue strength. Macek et al. considered that the larger pore sizes or closer-to-surface distance facilitates the fatigue initiation process [52]. For the same porosity level, specimen with smaller pores shows better fatigue strength than sample with bigger pores. It can be attributed to the fact that higher porosity or larger pore sizes reduce the fatigue crack propagation path and loosen the corresponding strength of the unsolid body that against the final fracture.

Correlation of fatigue strength with tensile strength

When comparing the fatigue strength with the tensile strength, normally for conventional steels, the fatigue strength can be proportionally expressed by the tensile strength [54]. When it comes to the *PBF-LB/M*

fabricate tool steels, the tensile strengths are higher in S3 than in C3, while the fatigue strengths are the opposite, i.e., $C3 > S3$. Accordingly, no correlation between the tensile strength and the fatigue strength is observed for the *PBF-LB/M* manufactured tool steels.

Summary/Conclusion

In the current research work, mechanical and fatigue investigation has been performed on different H13 variants produced by *PBF-LB/M* process. Some major conclusions can be drawn:

- The poor mechanical properties in the ordinary *PBF-LB/M* parts with as-built surface or parts of high porosity are owing to significant detrimental impacts from the rough as-built surface superimposed with tensile residual stresses and the high porosity.
- The deteriorated fatigue properties of *PBF-LB/M* generated H13 mainly come from the weakened matrix strength and the size of the largest lack of fusion defects. Despite the enhanced hardness and refined microstructure, which are beneficial for matrix strength, the presence of the typical microscopic solidification cracks, hot cracks and lack of fusion, a higher oxygen and nitrogen content, the weak connections of the scanned layers and some other microstructural factors reduce the strength of the matrix.
- The different scan patterns influence the matrix strengths and the distributions of the largest porous defects due to the different thermal gradients introduced. Furthermore, depending on the individual thermal distribution pattern, batch 2 and 3 of stripe pattern with a scan vector length of 10 mm show extensively large critical defects which prefer to occur in upper region of the horizontally build samples. Which indicates that the thermal history is dependent on position in the part despite constant process parameters.
- Negative porosity values are found with Archimedes method in the studied *PBF-LB/M* H13, which is attributed to the high amounts of denser retained austenite phase. The phase fraction of retained austenite can maybe be in turn evaluated

by porosity and the respective densities of austenite and martensite in future.

- Samples generated using a stripe pattern with 3-mm scan vector length presents the best overall tensile properties, and the strengths are comparable to the hardened conventional steel H13. Stripe pattern with a 10 mm length shows the possibility of generating samples with better fatigue properties, which almost reach the values of the hardened conventional steel H13.
- No direct relationships among the porosities, the tensile properties and the fatigue properties are revealed by the experiments.

Acknowledgements

The authors would like to express their cordial thanks to Deutsche Forschungsgemeinschaft DFG (German research foundation) for their financial support for the research work “Fatigue strength of by selective laser melting generated samples” with contract number 275999847. Sincere gratitude is also expressed to Mr. Raik Dörfert from BIAS (Institute of Applied Beam Technology, Bremen) for his contribution in the sample production. The feedback and support from Dr. Klaus Burkart from IWT (Leibniz Institute for Material-Oriented Technologies, Bremen) for his valuable suggestions and comments on improving the paper is also gratefully acknowledged.

Author contributions

Ms. Jun Zhang was responsible for the experiments carried out concerning the analysis and testing of samples. She analyzed all underlying reasons behind the findings and phenomena. She wrote the first version of the manuscript and discussed it with the other authors. Dr. Jens Schumacher contributed knowledge in the evaluation of the fatigue tests and discussed the results with Ms. Zhang. He also wrote the proposal of the underlying research project together with Prof. Dr. Brigitte Clausen. Prof. Clausen was in intense discussion throughout the whole writing process with Ms. Zhang. She further supported Ms. Zhang in the reviewing process of this paper.

Funding

Open Access funding enabled and organized by Projekt DEAL. The article was funded by Deutsche Forschungsgemeinschaft under the Grant No. (275999847).

Data availability

All data related to this release are held in an internal repository. Readers who are interested can be provided with these data upon request from the corresponding author (zhang@iwt-bremen.de, or clausen@iwt-bremen.de).

Declarations

Conflict of interest The authors declare that there is no conflict of interest.

Ethical approval No ethical approval was required for this research as it did not involve human tissue or any other parts of living organisms.

Open Access This article is licensed under a Creative Commons Attribution 4.0 International License, which permits use, sharing, adaptation, distribution and reproduction in any medium or format, as long as you give appropriate credit to the original author(s) and the source, provide a link to the Creative Commons licence, and indicate if changes were made. The images or other third party material in this article are included in the article's Creative Commons licence, unless indicated otherwise in a credit line to the material. If material is not included in the article's Creative Commons licence and your intended use is not permitted by statutory regulation or exceeds the permitted use, you will need to obtain permission directly from the copyright holder. To view a copy of this licence, visit <http://creativecommons.org/licenses/by/4.0/>.

References

- [1] The ASTM International Committee F42 (2015) Additive manufacturing - General principles - Terminology. <https://www.iso.org/obp/ui/#iso:std:iso-astm:52900:dis:ed-2:v1:en:erm:3.1.2>. Accessed 12 April 2021
- [2] Herderick E (2011) Additive manufacturing of metals: a review. *Mater Sci Technol Conf Exhib* 2(2011):1413–1425
- [3] Cormier D, Harrysson O, West H (2004) Characterization of H13 steel produced via electron beam melting. *Rapid Prototyp J* 10(1):35–41. <https://doi.org/10.1108/13552540410512516>
- [4] Wu L, Das S, Gridin W, Leuders S, Kahlert M, Vollmer M, Niendorf T (2021) Hot work tool steel processed by laser powder bed fusion: a review on most relevant influencing factors. *Adv Eng Mater* 23(7):2100049. <https://doi.org/10.1002/adem.202100049>
- [5] Bajaj P, Hariharan A, Kini A, Kürnsteiner P, Raabe D, Jägler EA (2020) Steels in additive manufacturing: a review of their microstructure and properties. *Mater Sci Eng A* 772:138633. <https://doi.org/10.1016/j.msea.2019.138633>
- [6] Brooks J, Robino C, Headley T, Goods S, Griffith M (1999) Microstructure and property optimization of LENS deposited H13 tool steel. In: *Proc 10th Solid Free Fabr Symp, The University of Texas at Austin, TX, USA*, pp 375–382. doi: <https://doi.org/10.26153/tsw/830>
- [7] Yan JJ, Chen MT, Quach WM, Yan M, Young B (2019) Mechanical properties and cross-sectional behavior of additively manufactured high strength steel tubular sections. *Thin-Walled Struct* 144:106158. <https://doi.org/10.1016/j.tws.2019.04.050>
- [8] Deirmina F, Al-Mangour B, Grzesiak D, Pellizzari M (2018) H13 - partially stabilized zirconia nanocomposites fabricated by high energy mechanical milling and selective laser melting. *Mater Des* 146:286–297. <https://doi.org/10.1016/j.matdes.2018.03.017>
- [9] Azizi H, Ghiaasiaan R, Prager R, Ghoncheh MH, Samk KA, Lausic A, Byleveld W, Phillion AB (2019) Metallurgical and mechanical assessment of hybrid additively - manufactured maraging tool steels via selective laser melting. *Addit Manuf* 27:389–397. <https://doi.org/10.1016/j.addma.2019.03.025>
- [10] Mertens R, Vrancken B, Holmstock N, Kinds Y, Kruth JP, van Humbeeck J (2016) Influence of powder bed preheating on microstructure and mechanical properties of H13 tool steel SLM parts. *Phys Procedia* 83:882–890. <https://doi.org/10.1016/j.phpro.2016.08.092>
- [11] Krell J, Röttger A, Geenen K, Theisen W (2018) General investigations on processing tool steel X40CrMoV5-1 with selective laser melting. *J Mater Process Technol* 255:679–688. <https://doi.org/10.1016/j.jmatprotec.2018.01.012>
- [12] Yan J, Song H, Dong Y, Quach WM, Yan M (2020) High strength (~2000 MPa) or highly ductile (~11%) additively manufactured H13 by tempering at different conditions. *Mater Sci Eng A* 773:138845. <https://doi.org/10.1016/j.msea.2019.138845>
- [13] Deirmina F, Peghini N, Al-Mangour B, Grzesiak D, Pellizzari M (2019) Heat treatment and properties of a hot work tool

- steel fabricated by additive manufacturing. *Mater Sci Eng A* 753:109–121. <https://doi.org/10.1016/j.msea.2019.03.027>
- [14] Wang M, Li W, Wu Y, Li S, Cai C, Wen S, Wei Q, Shi Y, Ye F, Chen Z (2019) High-temperature properties and microstructural stability of the AISI H13 hot-work tool steel processed by selective laser melting. *Metall Mater Trans B* 50(1):531–542. <https://doi.org/10.1007/s11663-018-1442-1>
- [15] Lee J, Choe J, Park J, Yu JH, Kim S, Jung ID, Sung H (2019) Microstructural effects on the tensile and fracture behavior of selective laser melted H13 tool steel under varying conditions. *Mater Charact* 155:109817. <https://doi.org/10.1016/j.matchar.2019.109817>
- [16] Nguyen V, Kim EA, Lee SR, Yun J, Choe J, Yang DY, Lee HS, Lee CW, Yu JH (2018) Evaluation of strain-rate sensitivity of selective laser melted H13 tool steel using nanoindentation tests. *Metals* 8(8):589. <https://doi.org/10.3390/met8080589>
- [17] Ren B, Lu D, Zhou R, Li Z, Guan J (2019) Preparation and mechanical properties of selective laser melted H13 steel. *J Mater Res* 34(08):1415–1425. <https://doi.org/10.1557/jmr.2019.10>
- [18] Le KQ, Tang C, Wong CH (2019) On the study of keyhole-mode melting in selective laser melting process. *Int J Thermal Sci* 145:105992. <https://doi.org/10.1016/j.ijthermalsci.2019.105992>
- [19] Kelly PM (2012) Crystallography of martensite transformations in steels. In: Pereloma E, Edmonds DV (eds) *Phase transformations in steels*. Woodhead Publishing Limited, Cambridge, pp 3–33. <https://doi.org/10.1533/9780857096111.1.3>
- [20] Wu L, Xia F, Gridin W, Florian F, S Leuders, Brenne F, Niendorf T (2018) Laser beam melting of H13 tool steel: from the evolution of microstructure to process simulation. Euro PM2018 Congress and Exhibition, Bilbao, Spain. https://www.researchgate.net/publication/329876286_Laser_beam_melting_of_H13_tool_steel_from_the_evolution_of_microstructure_to_process_simulation
- [21] Holzweissig MJ, Taube A, Brenne F, Schaper M, Niendorf T (2015) Microstructural characterization and mechanical performance of hot work tool steel processed by selective laser melting. *Metall Mater Trans B* 46(2):545–549. <https://doi.org/10.1007/s11663-014-0267-9>
- [22] Kou S (2002) *Welding metallurgy*, 2nd edn. Wiley, New Jersey. <https://doi.org/10.1002/0471434027>
- [23] Weman K (2003) *Welding processes handbook*. Woodhead Publishing, Cambridge
- [24] Kou S (2003) Solidification and liquation cracking issues in welding. *JOM* 55:37–42. <https://doi.org/10.1007/s11837-003-0137-4>
- [25] Kou S (2015) A criterion for cracking during solidification. *Acta Mater* 88:366–374. <https://doi.org/10.1016/j.actamat.2015.01.034>
- [26] Qin S, Bo Y, Herzog S, Hallstedt B, Kaletsch A, Broeckmann C (2022) influence of process parameters on porosity and hot cracking of AISI H13 fabricated by laser powder bed fusion. *Powders* 1(3):184–193. <https://doi.org/10.3390/powders1030012>
- [27] Xia C, Kou S (2021) Calculating the susceptibility of carbon steels to solidification cracking during welding. *Metall Mater Trans B* 52:460–469. <https://doi.org/10.1007/s11663-020-2021-5>
- [28] Deirmina F, Davies PA, Dixit N, Siriki R, Pellizzari M (2022) Production and characterization of a modified hot work tool steel by laser powder bed fusion. *Metall Mater Trans A* 53:2642–2651. <https://doi.org/10.1007/s11661-022-06694-2>
- [29] Cloots M, Uggowitzer PJ, Wegener K (2016) Investigations on the microstructure and crack formation of IN738LC samples processed by selective laser melting using gaussian and doughnut profiles. *Mater Des* 89:770–784. <https://doi.org/10.1016/j.matdes.2015.10.027>
- [30] Dovggy B, Simonelli M, Pham MS (2021) Alloy design against the solidification cracking in fusion additive manufacturing: an application to a FeCrAl alloy. *Mater Res Lett* 9(8):350–357. <https://doi.org/10.1080/21663831.2021.1922945>
- [31] Hyer H, Zhou L, Mehta A, Park S, Huynh T, Song S, Bai Y, Cho K, McWilliams B, Sohn Y (2021) Composition-dependent solidification cracking of aluminum-silicon alloys during laser powder bed fusion. *Acta Mater* 208:116698. <https://doi.org/10.1016/j.actamat.2021.116698>
- [32] Prasad K, Obana M, Ishii Y, Ito A, Torizuka S (2021) The effect of laser scanning strategies on the microstructure, texture and crystallography of grains exhibiting hot cracks in additively manufactured Hastelloy X. *Mech Mater* 157:103816. <https://doi.org/10.1016/j.mechmat.2021.103816>
- [33] Liu J, Yin B, Sun Z, Wen P, Zheng Y, Tian Y (2021) Hot cracking in ZK60 magnesium alloy produced by laser powder bed fusion process. *Mater Lett* 301:130283. <https://doi.org/10.1016/j.matlet.2021.130283>
- [34] Sun Z, Tan XP, Descoins M, Mangelinck D, Tor SB, Lim CS (2019) Revealing hot tearing mechanism for an additively manufactured high-entropy alloy via selective laser melting. *Scr Mater* 168:129–133. <https://doi.org/10.1016/j.scriptamat.2019.04.036>
- [35] Mazur M, Brincat P, Leary M, Brandt M (2017) Numerical and experimental evaluation of a conformally cooled H13 steel injection mould manufactured with selective laser

- melting. *Int J Adv Manuf Technol* 93(1–4):881–900. <https://doi.org/10.1007/s00170-017-0426-7>
- [36] Yan JJ, Zheng DL, Li HX, Jia X, Sun JF, Li YL, Qian M, Yan M (2017) Selective laser melting of H13: microstructure and residual stress. *J Mater Sci* 52(20):12476–12485. <https://doi.org/10.1007/s10853-017-1380-3>
- [37] AlMangour B, Grzesiak D, Yang JM (2017) Selective laser melting of TiB₂/H13 steel nanocomposites: influence of hot isostatic pressing post-treatment. *J Mater Process Technol* 244:344–353. <https://doi.org/10.1016/j.jmatprotec.2017.01.019>
- [38] Park JS, Park JH, Lee MG, Sung JH, Cha KJ, Kim DH (2016) Effect of energy input on the characteristic of AISI H13 and D2 tool steels deposited by a directed energy deposition process. *Metall Mater Trans A Phys Metall Mater Sci* 47:2529–2535. <https://doi.org/10.1007/s11661-016-3427-5>
- [39] Bohlen A, Freiße H, Hunkel M, Vollertsen F (2018) Additive manufacturing of tool steel by laser metal deposition. *Procedia CIRP* 74:192–195. <https://doi.org/10.1016/j.procir.2018.08.092>
- [40] Xue L, Chen J, Wang SH (2013) Freeform laser consolidated H13 and CPM 9V tool steels. *Metallogr Microstruct Anal* 2:67–78. <https://doi.org/10.1007/s13632-013-0061-0>
- [41] Mazumder J, Choi J, Nagarathnam K (1997) The direct metal deposition of H13 tool steel for 3-D components. *JOM* 49:55–60. <https://doi.org/10.1007/BF02914687>
- [42] Choi J, Chang Y (2005) Characteristics of laser aided direct metal/material deposition process for tool steel. *Int J Mach Tool Manuf* 45:597–607. <https://doi.org/10.1016/j.ijmactools.2004.08.014>
- [43] Ali Y, Barnikol-Oettler S, Reimann J, Hildebrand J, Henckell P, Bergmann JP (2019) Wire arc additive manufacturing of hot work tool steel with CMT process. *J Mater Process Technol* 269:109–116. <https://doi.org/10.1016/j.jmatprotec.2019.01.034>
- [44] Pinkerton AJ, Li L (2005) Direct additive laser manufacturing using gas- and wateratomised H13 tool steel powders. *Int J Adv Manuf Technol* 25:471–479. <https://doi.org/10.1007/s00170-003-1844-2>
- [45] Mazumder J, Schifferer A, Choi J (1999) Direct materials deposition: designed macro and microstructure. *Mater Res Innov* 3:118–131. <https://doi.org/10.1007/s100190050137>
- [46] Hofmeister W, Griffith M, Ensz M, Smugeresky J (2001) Solidification in direct metal deposition by LENS processing. *JOM* 53:30–34. <https://doi.org/10.1007/s11837-001-0066-z>
- [47] Cottam R, Wang J, Luzin V (2014) Characterization of microstructure and residual stress in a 3D H13 tool steel component produced by additive manufacturing. *J Mater Res* 29:1978–1986. <https://doi.org/10.1557/jmr.2014.190>
- [48] Rafi HK, Karthik NV, Gong H, Starr TL, Stucker BE (2013) Microstructures and mechanical properties of ti6al4v parts fabricated by selective laser melting and electron beam melting. *J Mater Eng Perform* 22(12):3872–3883. <https://doi.org/10.1007/s11665-013-0658-0>
- [49] Kahlert M, Brenne F, Vollmer M, Niendorf T (2021) Influence of microstructure and defects on mechanical properties of AISI H13 manufactured by electron beam powder bed fusion. *J Mater Eng Perform* 30(9):6895–6904. <https://doi.org/10.1007/s11665-021-06059-7>
- [50] Garcias JF, Martins RF, Branco R, Marciniak Z, Macek W, Pereira C, Santos C (2021) Quasistatic and fatigue behavior of an AISI H13 steel obtained by additive manufacturing and conventional method. *Fatigue Fract Eng Mater Struct* 44:3384–3398. <https://doi.org/10.1111/ffe.13565>
- [51] Pellizzari M, AlMangour B, Benedetti M, Furlani S, Grzesiak D, Deirmina F (2020) Effects of building direction and defect sensitivity on the fatigue behavior of additively manufactured H13 tool steel. *Theor Appl Fract Mech* 108:102634. <https://doi.org/10.1016/j.tafmec.2020.102634>
- [52] Macek W, Martins RF, Branco R, Marciniak Z, Szala M, Wroński S (2022) Fatigue fracture morphology of AISI H13 steel obtained by additive manufacturing. *Int J Fract* 235:79–98. <https://doi.org/10.1007/s10704-022-00615-5>
- [53] Dörfert R, Zhang J, Clausen B, Freiße H, Schumacher J, Vollertsen F (2019) Comparison of the fatigue strength between additively and conventionally fabricated tool steel 1.2344. *Addit Manuf* 27:217–223. <https://doi.org/10.1016/j.addma.2019.01.010>
- [54] Murakami Y (2002) *Metal fatigue: effects of small defects and nonmetallic inclusions*. Elsevier, Oxford
- [55] Narvan M, Al-Rubaie KS, Elbestawi M (2019) Process-structure-property relationships of AISI H13 tool steel processed with selective laser melting. *Materials* 12(14):2284. <https://doi.org/10.3390/ma12142284>
- [56] He Y, Zhong M, Beuth J, Webler B (2020) A study of microstructure and cracking behavior of H13 tool steel produced by laser powder bed fusion using single-tracks, multi-track pads, and 3D cubes. *J Mater Process Technol* 286:116802. <https://doi.org/10.1016/j.jmatprotec.2020.116802>
- [57] Kruth JP, Mercelis P, Vaerenbergh JV, Froyen L, Rombouts M (2005) Binding mechanisms in selective laser sintering and selective laser melting. *Rapid Prototyp J* 11(1):26–36. <https://doi.org/10.1108/13552540510573365>
- [58] Gu D, Shen Y (2009) Balling phenomena in direct laser sintering of stainless steel powder: metallurgical mechanisms

- and control methods. *Mater Des* 30(8):2903–2910. <https://doi.org/10.1016/j.matdes.2009.01.013>
- [59] Townsend A, Senin N, Blunt L, Leach RK, Taylor JS (2016) Surface texture metrology for metal additive manufacturing: a review. *Precis Eng* 46:34–47. <https://doi.org/10.1016/j.precisioneng.2016.06.001>
- [60] Mercelis P, Kruth JP (2006) Residual stresses in selective laser sintering and selective laser melting. *Rapid Prototyp J* 12(5):254–265. <https://doi.org/10.1108/13552540610707013>
- [61] Wu L, Gridin M, Leuders S, Niendorf T (2019) The application of H13-type steel in LBM process: sensitivity to the powder condition and preheating temperature. In: *Proc Euro PM 2019: Int Powder Metall Congress and Exhibition*, Maastricht, The Netherlands, pp 1–6
- [62] Kou S (2015) A simple index for predicting the susceptibility to solidification cracking. *Weld J* 94:374s–388s. http://app.aws.org/wj/supplement/WJ_2015_12_s374.pdf
- [63] S-Point (2018) 1.2344. https://www.s-point.at/media/wysiwyg/service/downloads/werkstoffdatenblaetter/S-Point_1.2344.pdf. Accessed 06 December 2022
- [64] AZO Materials (2013) H13 Tool Steel - Chromium Hot-Work Steels. <https://www.azom.com/article.aspx?ArticleID=9107>. Accessed 06 December 2022
- [65] Erpro Group (2019) Material Data Sheet Stainless Steel 316L / 1.4404 / A276. https://erpro-group.com/wp-content/uploads/2019/04/Fe_316L.pdf. Accessed 06 December 2022
- [66] Thyssenkrupp Materials (2017) Stainless Steel 316L 1.4404. <https://www.thyssenkrupp-materials.co.uk/stainless-steel-316l-14404.html>. Accessed 06 December 2022
- [67] SLM-Solutions (2023) Tool Steel 1.2344 / A681 H13 / H13. https://www.slm-solutions.com/fileadmin/Content/Powder/MDS/MDS_Fe-Alloy_H13_0219_EN.pdf. Accessed 07 December 2022
- [68] Lyassami M, Shahriari D, Fredj EB, Morin JB, Jahazi M (2018) numerical simulation of water quenching of large size steel forgings: Effects of macrosegregation and grain size on phase distribution. *J Manuf Mater Process* 2(2):34. <https://doi.org/10.3390/jmmp2020034>
- [69] Cho YG, Kim JY, Cho HH, Cha PR, Suh DW, Kon Lee J, Han HN (2015) Densities of austenite and ferrite phase as a function of temperature and chemical composition. *PLOS ONE Dataset*. <https://doi.org/10.1371/journal.pone.0035987.t002>
- [70] Muschkopp (2015) Densities of different phases of steel (austenite, bainite). <https://engineering.stackexchange.com/questions/3803/densities-of-different-phases-of-steel-austenite-bainite>. Accessed 06 December 2022
- [71] Qu R, Zhang P, Zhang Z (2014) Notch effect of materials: strengthening or weakening? *J Mater Sci Technol* 30(6):599–608. <https://doi.org/10.1016/j.jmst.2014.04.014>
- [72] Straffelini G, Menapace C, Molinari A (2002) Interpretation of effect of matrix hardening on tensile and impact strength of sintered steels. *Powder Metall* 45:2. <https://doi.org/10.1179/003258902225002587>
- [73] Milan MT, Bowen P (2004) Tensile and fracture toughness properties of SiCp reinforced Al alloys: effects of particle size, particle volume fraction, and matrix strength. *J Mater Eng Perform* 13:775–783. <https://doi.org/10.1361/10599490421358>

Publisher's Note Springer Nature remains neutral with regard to jurisdictional claims in published maps and institutional affiliations.